UNIAXIAL PRESSURE INDUCED STRUCTURAL TRANSITIONS IN MOLYBDENUM DITELLURIDE

Imiya Mudiyanselage Erandi Sachinthanie

Kandy, Sri Lanka

Bachelor of Science in Physics Honors, University of Peradeniya, 2021

A Thesis submitted to the Graduate Faculty

of the University of Virginia in Candidacy for the Degree of

Master of Science

Department of Physics

University of Virginia

June 2024

Advisor D. Louca, Chair

Second J. Teo

Third U. Chatterjee

Abstract

$MoTe_2$ is a versatile transition metal dichalcogenide known for its intriguing electronic properties, including a high electron mobility and significant magnetoresistance, making it a promising material for advanced electronic and spintronic applications. It is also a type II Weyl semimetal with three different polytype forms; monoclinic, orthorhombic, and hexagonal. Its crystalline structure is composed of two-dimensional layers, each layer made of Mo^{4+} ions and Te^{-2} ions connected by strong covalent bonding in a zig-zag pattern. The weak interlayer coupling, known as van der Waals (vdW), enables the layers to slide over each other, rearranging the structure and allowing transitions across the different polytypes. Electronic and topological properties have been found to differ among the three polytypes.

$MoTe_2$ undergoes a topological phase transition when cooled from approximately 350 K, transitioning from a monoclinic 1T′ to an orthorhombic T_d structure at lower temperatures, with the phase transition nominally occurring around 250 K. The topological properties of $MoTe_2$ can be influenced by external factors such as external fields, defects, disorder, chemical doping, and pressure. In this thesis, the structural phase transition of $MoTe_2$ under strain is explored using elastic neutron scattering. Moreover transport across the vdW layers is measured for the first time.

Transport measurements were conducted in two planes: the in-plane (layer growth plane) and the out-of-plane (layer stacking plane). In-plane transport measurements revealed a sudden increase in the gradient of the resistivity curve, as a function of

temperature, indicating the point at which the structural transition occurs. The in-plane resistivity curve forms a closed hysteresis loop between 200 and 270 K, within which the structural transition occurs. In contrast, the out-of-plane resistivity measurements, displayed a broad, open hysteresis loop from 200 up to 350 K. This observation accounts for layer sliding in the out-of-plane direction, where each layer must be perfectly positioned after sliding to form a specific crystal structure. Broad diffuse scattering occurs within this temperature range.

Applying pressure to $MoTe_2$ alters the temperature at which phase transitions occur, affecting its electronic structure and potentially leading to new topological phases. In this thesis, uniaxial strain was applied using a mechanical pressure cell in the out-of-plane direction of a cubic $MoTe_2$ crystal, followed by elastic neutron scattering. An increase in applied pressure/force led to lowering of the structural phase transition temperature. Neutron scattering experiment revealed changes in the intensities of the out-of-plane 201 and $20\bar{1}$ peaks under strain. Variation in the intensity of these peaks as a function of pressure was observed, and further measurements will be conducted to precisely clarify the origin of these results. Moreover the broad diffuse scattering spectrum will be discussed by analyzing the diffuse scattering along the h0l and 0kl planes in contrast to the hk0 plane, where there is no diffuse scattering using the data aquired from TOPAZ, a high-resolution single-crystal diffractometer.

Dedication

Dedicated to my parents, who've been with me through thick and thin...

Acknowledgments

In many ways this incredible journey in making this research project a success, can be compared to sailing through a vast sea of knowledge and experience. There were seemingly endless times where the sea got daring and rough, almost making myself get lost among its daunting waves, pressing me to lower the sails and to give up. But there was always a bright beam of light which led me to the shore, safe and sound, guiding me patiently through this experience, leading me to obtain new victories every day, no matter how small they seem. This invaluable guidance was offered to me by my encouraging supervisor, Prof. Despina Louca,who led me to obtain all my goals successfully. She was always there for me day and night with her invaluable advice, experience, incomparable knowledge, dedication and support. I am lost for words when paying my gratitude for her and I thank her whole heartedly for believing in me.

I would like to express my deepest gratitude to Professor Sachith Dissanayake for his invaluable assistance during the neutron scattering experiment at ORNL. His willingness to accompany me, dedicate his time, and provide expert guidance throughout the experiment and analysis process was instrumental to the success of this work. I am also profoundly

grateful to Professor Songxue Chi, the scientist in charge of the HB3 triple axis neutron scattering spectrometer, for his significant help in ensuring the experiment was completed within the allocated time frame. His willingness to sacrifice time from his subsequent experiment demonstrated exceptional generosity and commitment. Additionally, I would like to extend my heartfelt thanks to Dr. Eleanor M. Clements for her unwavering support and dedication, coming by day and night, always on foot, whenever needed. All of the staff at the HB3, triple axis neutron spectrometer setup should be thanked wholeheartedly, for the support offered during the 10 days of our experiment. Their collective efforts, mentorship, and sacrifices have been crucial in the successful completion of this research.

I would also like to thank Dr John Scheeloch, our postdoctoral supervisor for always helping out, explaining theoretical and experimental procedures, willing to lend a hand at any given moment, no matter how many times I barge into his office at a given day. Dr.Armando di Biase should also be thanked for his invaluable guidance during the final days of my research. I am profoundly grateful to my undergraduate research supervisor, Dr. Chani Perera, and my mentor, Dr. Varuni Seneviratne, for their unwavering emotional support during my two-year period at UVa. Their presence and encouragement during moments of personal

struggle were a source of immense strength and comfort. Dr. Perera's and Dr. Seneviratne's compassion, understanding, and guidance helped me persevere through challenging times, and their belief in my abilities inspired me to overcome obstacles and continue striving for excellence. I am deeply thankful for their kindness and support, which have been instrumental in my academic and personal growth. I would like to extend my heartfelt gratitude to Prof. J. Teo and Prof. U. Chatterjee for serving as review panel members at my thesis defense. I deeply appreciate their willingness to dedicate their time and share their invaluable comments and insights. Their expertise and constructive feedback have been instrumental in enhancing the quality of my research, and I am sincerely thankful for their support and guidance throughout this process.

Last, but not certainly least, my loving parents: Yasho and Imiya Dayarathna, my sister: Imiya Chathuranika, my brother-in-law/brother (soon-to-be Dr.) Anuruddha Rathnayaka and my wonderful life partner, Thisara Chathuranga should also be thanked for encouraging me whenever I felt I was lagging behind and for always being my cheerleading squad. My fellow batch mates were always supportive in every possible way and it is a pleasure to thank them. I would also take this opportunity to thank my friends who helped me through thick and thin. My kitten Shock should also be lovingly mentioned for helping me in balancing out

my mentality. I sincerely apologize to any personnel whose name was not mentioned in here, who had helped me in any way to make this project a success, thank you very much.

Contents

List of Figures

Chapter 1

Introduction

1.1 Properties of $MoTe_2$ as a Weyl semimetal

A topological Weyl semimetal exhibits Weyl fermions and possesses non-trivial topological properties in its electronic band structure.[1] Weyl semimetals are characterized by the presence of pairs of Weyl points in their Brillouin zone, where the conduction and valence bands touch linearly at a singular Weyl or Dirac point, leading to the emergence of massless quasi particles known as Weyl fermions.[2] In a topological Weyl semimetal, Weyl points arise due to the breaking of certain symmetries, such as time-reversal or inversion. These points are topologically protected and cannot be removed from the electronic band structure without further breaking other symmetries, making them robust against small perturbations and disorder[3] An important characteristic of Weyl semimetals is the emergence of Fermi surface arcs. Fermi arcs are open contours formed by the surface states on the surface Brillouin zone. They connect pairs of surface projections of Weyl points with opposite chiralities.[2] Fermi arcs are distinct from conventional Fermi surfaces, which are closed contours in momentum space.[4] Fermi arcs are typically observed by angle-resolved photoemission

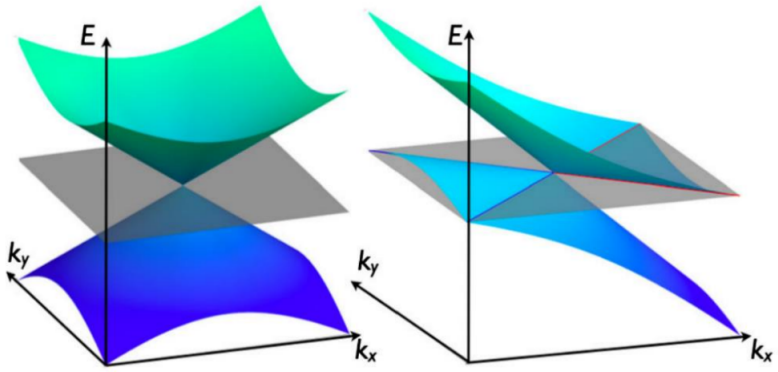

Figure 1.1: Conventional type-I Weyl point with point like Fermi surface (left) vs. type-II Weyl point, which is the contact point between electron and hole pockets (right).The figure is from Ref.[5].

spectroscopy (ARPES) experiments as disconnected segments of Fermi surface. There are two types of Weyl semimetals: type-I and type-II. Both types have contact points of electrons and holes. [6] The Fermi surface dispersions are shown in Figure 1.1. $MoTe_2$ has been studied due to its unique electronic properties, particularly as a type-II Weyl semimetal. In quantum field theory, particles and their corresponding antiparticles often exhibit a property called chirality, which describes their handedness or the way they spin relative to their direction of motion. Chiral particles can be either left-handed (LH) or right-handed (RH), depending on whether their spin is aligned or anti-aligned with their momentum.[7] The presence of Weyl points in $MoTe_2$ leads to the manifestation of chiral anomaly, a phenomenon in which the conservation of chiral charge is violated in the presence of external electric and magnetic fields.[8] This results in the generation of a chiral current perpendicular to both the electric and magnetic fields, leading to unusual transport properties such as negative magnetoresistance.[8] $MoTe_2$ also possesses topological surface states associated with

its Weyl semimetal phase.[2] These surface states are protected by the non-trivial topology of the bulk electronic band structure and exhibit unique electronic properties.

Spintronics, extreme magnetoresistance (XMR), pressure-induced change in superconductivity transition temperature, Mott physics, quantum spin hall (QSH) insulating state, charge density waves (CDW), quantum computing, and topological electronics are some of the various applications.[9,10] The ability to manipulate and control Weyl fermions and their associated phenomena in $MoTe_2$ could lead to the development of next-generation electronic devices with enhanced performance and functionality. [10] Bulk $MoTe_2$ crystals consist of 2D layers made up of Mo^{4+} and Te^{2-} ions, connected in a zig-zag pattern via strong covalent bonds. A $MoTe_2$ crystal consists of 2D layers stacked on top of each other, with weak vdW bonds holding the layers together. The layers follow an A/B-type stacking sequence. [11] A crystal can be exfoliated into single layers with a thickness of one unit cell. Changes to this stacking sequence result in different polytypes of $MoTe_2$ including, the hexagonal (α-phase or 2H phase), monoclinic (β-phase or 1T$'$ phase) and the orthohombic (γ-phase or T_d phase).[10] The variations in the unit cell structures for the T_d phase and the 1T$'$ phase are shown in Figure 1.2.

The structure of $MoTe_2$ is characterized by the A/B stacking sequence and the distance along the a-direction (layer growth direction) between the centers of inversion symmetry of neighboring layers. Typically, this distance corresponds to the spacing

between adjacent metal atoms in the layers [1]. The key observation centers around the nearly identical arrangements of atom pairs between adjacent layers. In an ideal scenario, applying an inversion operation to the structure would map a specific layer onto itself while also transforming surrounding layers between different stacking sequences (A to B and vice versa). This process reflects the alternating order of A/B stacking operations, where A and B represent equivalent symmetry operations. As a result, the distance between any two adjacent layers remains consistent regardless of whether they follow an A or B stacking pattern. [12]

The stable structure of $MoTe_2$ has hexagonal symmetry at room temperature.[12] The monoclinic structure is not energetically favourable at room temperature, but rapid quenching from high temperatures can trap the monoclinic structure at room temperature.[13] From the monoclinic phase, a structural phase transition can be observed in bulk $MoTe_2$ around 250 K, where the structure changes to a low temperature orthorhombic phase upon cooling. [12].

The distinction between the orthorhombic and monoclinic states is evident in their layer stacking configurations. In Figure 1.2(b), the T_d structure exhibits an AA layer pattern, where each layer aligns directly with the next. This stacking involves a translation along the c axis by half a lattice constant and reflections across the a and b directions.[11]. On the other hand, Figure 1.2(a) illustrates the 1T′ phase, characterized by an AB layer arrangement. Here, B layers undergo an additional shift of approximately ± 0.15 lattice units along the a direction, alternating between even

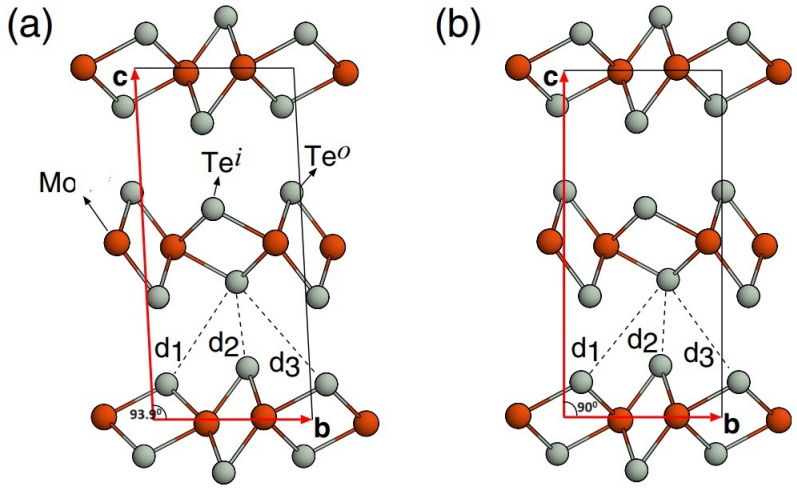

Figure 1.2: Schematic atomic structures of (a) the β and (b) the γ phase of $MoTe_2$ projected on the bc plane. b and c denote unit vectors of the primitive unit cell (a is perpendicular to the bc plane). The solid line indicates the unit cell. The dark (red) and bright (gray) circles represent Mo and Te atoms, respectively. Te atom being close to (away from) the transition metal plane is denoted by $Te^{i(o)}$, respectively. For the $\beta(\gamma)$ phase, $d_1 < d_3$ ($d_1 > d_3$). The angle between b and c is (a) 93.9° and (b) 90°. The figure is from Ref.[10].

and odd positions in the layer sequence.[11] While this is a simplified description of the 1T′ structure and overlooks some intralayer distortions compared to T_d, it highlights the fundamental choice of layer placement at each interlayer boundary. The extra shifts in 1T′ lead to a monoclinic unit cell tilt with an angle between the b and c directions of a unit cell of approximately 93.9 degrees. [11]

As temperatures rise, the T_d^* phase emerges, characterized by a pseudo-orthorhombic structure with a four-layer unit cell, contrasting with the two-layer unit cells of 1T′ and T_d phases. [12] The layer stacking in T_d^* follows an $AABB$ sequence, as depicted in Figure 1.3. The transition from T_d to T_d^* upon warming does not involve disorder.[12] Further warming from T_d^* to 1T′ reveals diffuse scattering. In contrast, cooling from

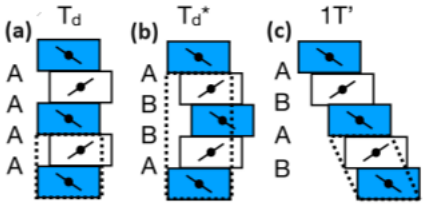

Figure 1.3: Structural arrangements of $MoTe_2$ for the T_d, T_d^* and 1T′ phases. (a)The T_d phase with an angle of 90° between the b and c axes have layers perfectly aligned on top of each other in the stacking order. (b) The intermediate T_d^* has a four-layer unit cell also exhibiting the unit cell doubling feature. (c) The 1T′ phase goes back to two-layered unit cell structure, with an angle of 93.9° between the b and c axes. The figure is from Ref.[12].

1T′ to T_d does not pass through the T_d^* phase; instead, only diffuse scattering occurs, indicating a frustrated inclination towards $AABB$ layer ordering. [12] The layer stacking sequences for the T_d, T_d^* and 1T′ are shown in Figure 1.3. In comparison with the T_d phase, T_d^* has additional Bragg peaks at half integer L values, giving rise to an orthorhombic structure. [11] It has also been discovered that T_d^* is centrosymmetric (having symmetry with a central point) in the same P21/m space group as the 1T′ phase.[12]

1.2 Extreme magnetoresistance

In addition to the nontrivial topological band structure, $MoTe_2$ has other interesting properties, one of which is extreme magnetoresistance. Magnetoresistance refers to the change in electrical resistance of a material under the influence of an external magnetic field.[1] The applications of this behavior can be found in memory devices, hard drives and spintronics [1]. Magnetoresistance (MR) is typically expressed as

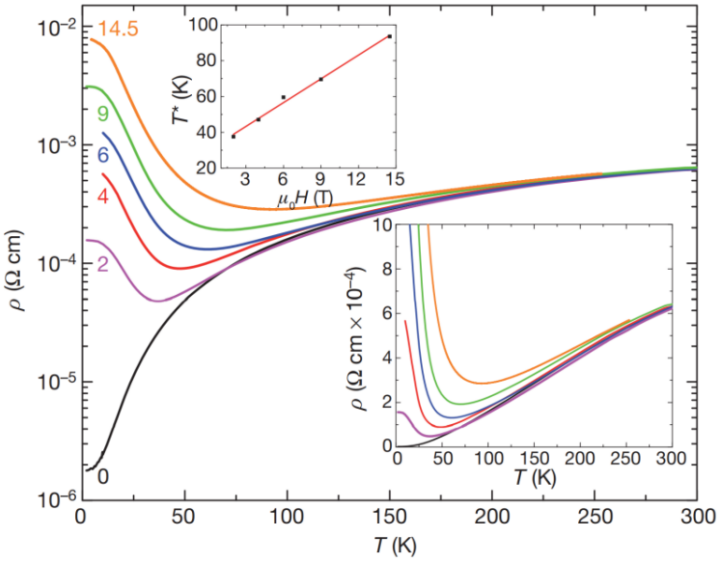

Figure 1.4: Temperature and magnetic field dependence of the XMR in WTe_2, when the current is applied along the b-axis (W-chain direction) and magnetic field is parallel to c-axis (perpendicular to the layers).The figure is from Ref [23].

a percentage and calculated using the relation $\frac{\rho(H)-\rho(0)}{\rho(0)}$. Here, $\rho(H)$ represents the resistance with an applied magnetic field H, and $\rho(0)$ is the resistance without any magnetic field. Extreme Magnetoresistance (XMR) materials, such as $MoTe_2$, are characterized by their temperature-dependent resistivity $\rho(T)$, which shows a distinct turn-on behavior.[14] When a magnetic field is applied, the material's resistivity initially follows a similar trend to its behavior without a magnetic field until it reaches the turn-on temperature. Below this temperature, the resistivity begins to increase significantly. For example, in WTe_2, a non-saturating XMR was observed. Shown in Fig. 1.4 is the electrical resistivity as a function of temperature for WTe_2 under different magnetic fields that shows that the XMR effect in WTe_2 can be turned on at low temperatures with an external magnetic field. Such XMR in WTe_2 has been

explained by the nearly perfect balanced electron-hole populations in the T_d phase.

Dual electron and hole pockets are observed in $MoTe_2$ within the X-Γ-X direction, with a temperature-induced Lifshitz transition around $T \approx 160$ K [16]. A Lifshitz transition is a phase transition in the electronic structure of a material that occurs due to a change in the Fermi surface topology. In simpler terms, it involves a rearrangement of the electronic states near the Fermi level.[15]. A band gap opening at the $'$turn-on$'$ temperature suggests two possible Fermi surface reconstructions, one around 150 K and the other around 60 K [1]. The first-principles calculations can be used to theoretically validate the Fermi energy splittings due to the hole pockets. The changes in the sizes of the electron and hole pockets will also influence the carrier concentrations, for example, when the temperature is decreased, the hole concentration increases. The perfect electron - hole compensation gives rise to the XMR in T_d-$MoTe_2$, of which the driving factor is the electronic structural change around 60 K. By introducing variable tensile strain with the use of an electric field on a piezoelectric stack, it has been shown that an anisotropy in the MR is observed with symmetry breaking in the T_d and 1T$'$ phases, with the result varying on whether a or b direction is considered [13]. Alterations in the band structures near the Γ point and along the Y→ Γ direction present an avenue for unique manipulation of band overlap via tensile strain. When strain is exerted along the a axis, band shifts result in a slightly diminished density of states (DOS) around the Fermi energy (E_F). Conversely, ap-

plication of strain along b induces band shifts in the opposite direction, leading to an apparent increase in DOS at E_F.[17] Consequently, it is anticipated that strain will alter the orbital configuration of both electron and hole pockets, thereby influencing the electron scattering between different pockets. [17]

When uniaxial strain is applied to $MoTe_2$, the resulting structural transition modifies its electronic band structure, influencing the Weyl points and the density of states near the Fermi level. This change in the electronic structure affects the carrier concentration and mobility, which in turn impacts the magnetoresistance. Each structural phase of $MoTe_2$ has unique electronic properties that determines its magnetoresistance behavior. For instance, the T_d phase has been known to have a higher magnetoresistance compared to the 1T′ phase, and therefore, a strain-induced transition to the T_d phase will enhance the XMR. By carefully controlling the strain, it is possible to modulate the magnetoresistance characteristics of $MoTe_2$, providing a tunable mechanism for optimizing its electronic properties.

1.3 Superconductivity

Electrical resistivity measurements show that T_d-$MoTe_2$ exhibits superconductivity at a transition temperature T_c of 0.01 K [18]. A dome-shaped superconducting behavior has been observed with varying pressure, as shown in Figure 1.5. The electrical resistivity of $MoTe_2$ under pressure is depicted in Figure 1.6. In panel (a) of Figure

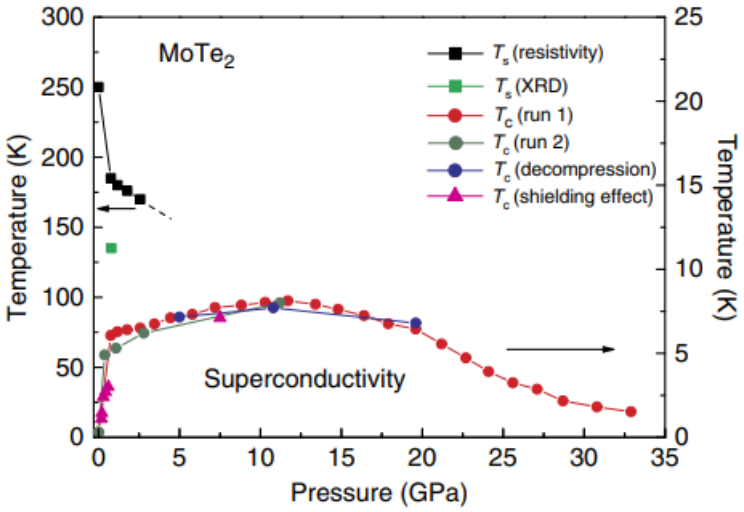

Figure 1.5: Dome shaped superconductivity behaviour in $MoTe_2$. The black and green squares represent the structural phase transition temperature obtained from resistivity and single-crystal synchrotron x-ray diffraction data. The red, blue and olive circles represent the T_c extracted from various electrical resistance measurements, and the magenta triangles represent the T_c determined from the magnetization measurements. The figure is from Ref.[18].

1.6, the resistivity is shown as a function of temperature ranging from 0.7 to 11.7 GPa, while panel (b) of Figure 1.6 illustrates the range from 11.7 to 34.9 GPa. Initially, T_c increases with rising pressure, peaking at $T_c = 8.2$ K at 11.7 GPa, which is about 80 times larger than the ambient pressure value. [19] However, further pressure increment gradually suppresses the zero-resistance-point T_c. No signs of superconductivity has been reported in the 2H phase of $MoTe_2$ for pressures up to 40 GPa, although it becomes metallic at a pressure of 15 GPa [19]. Uniaxial strain changes the electronic band structure of $MoTe_2$, influencing the density of states at the Fermi level by altering the spacing and overlap of electronic bands. [20]

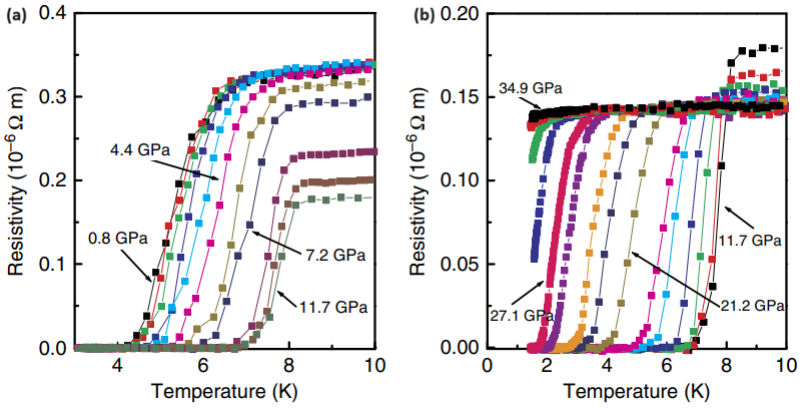

Figure 1.6: Electrical resistivity of $MoTe_2$ as a function of temperature and pressure, showing the increments in T_c. (a) Electrical resistivity as a function of temperature for pressures of 0.76 - 34.9 GPa. The anomaly associated with the structural transition is completely suppressed with increasing pressure. (b) Electrical resistivity as a function of temperature for pressures of 0.7 - 11.7 GPa. Clear electrical resistivity drops and zero-resistance behaviour are apparent. T_c increases under increasing pressure and a dome-shaped superconducting phase in pressure–temperature space is observed for the maximum superconducting transition temperature corresponding to $T_c = 8.2$ K at 11.7 GPa. The figure is from Ref.[18].

1.4 Outline of the thesis

The research described in the thesis mainly consists of the neutron scattering and transport measurements exploring the structural phase transitions in $MoTe_2$. The objective is to find the effect of uniaxially applied pressure in: a (growth direction), b (the in-plane direction perpendicular to the growth direction and c (layer stacking direction) to the structural phase transition temperature of high temperature monoclinic to low temperature orthorhombic, which under ambient conditions appears around 250 K.

The following chapters of the thesis are organized as follows. Chapter 2 will focus on the details of the neutron scattering techniques including the physical concepts behind

the experimental procedure of inelastic neutron scattering. Chapter 3 will present the detailed synthesis and characterization of $MoTe_2$. The flux growth method, which was used to synthesize monoclinic phase $MoTe_2$ crystals will be discussed along with few other types of synthesis techniques. Characterization using transport measurements taken from the Physical Property Measurement System (PPMS) will also be discussed. Application of the neutron scattering techniques discussed in Chapter 2 will be given in detail, from preparation of samples, sample alignment before loading to the pressure cell and the loading of the pressure stick into the cryostat. In Chapter 4, results of the transport measurements will be discussed in-plane and out-of-plane. Theoretical explanations to why these results can be seen will also be discussed in detail. Chapter 5 will provide an insight to the results of the uniaxial strain experiment done with inelastic neutron scattering. Both in-plane and out-of-plane results will be broadly discussed, along with a theoretical explanation to them. Chapter 6 and 7 will present the discussion and a brief conclusion of the thesis respectively.

Chapter 2

Neutron scattering

2.1 Introduction

Neutron scattering is a powerful experimental technique used in condensed matter physics, materials science, chemistry, and biology to probe the structure, dynamics, and interactions of materials at the atomic and molecular level. It involves the scattering of neutrons off the atomic nuclei within a material, providing valuable information about its properties. Neutrons are ideal probes for studying materials because they have properties that make them sensitive to different aspects of a material's structure and behavior.[21] Neutrons are electrically neutral, allowing them to penetrate deeply into materials without being affected by the electric fields due to surrounding electrons. The mass of a neutron is about the size of an hydrogen atom, making the scattering process sensitive to probing the nuclei.[22] Additionally, the de Broglie wavelength of thermal neutrons (typically ranging from 5 to 100 meV) closely matches the inter atomic spacing found in solids, which typically lies on the order of 10^{-10} meters.[14] This phenomenon allows thermal neutrons to use interference effects, making it easier to detect microscopic structures within the scattering

system. Neutrons possess a magnetic moment, typically measured at 1.913 nuclear magnetons (μ_N), and primarily interact with the magnetic moments of electrons, protons, nuclear spin and electromagnetic fields within the nucleus.[14] This interaction provides valuable insights into the magnetic structure of materials. Moreover, the energy of thermal neutrons closely aligns with that of numerous excitations within solids. Through inelastic neutron scattering, a technique wherein neutrons undergo energy changes during the scattering process, energy of these excitations can precisely be determined.[22]

Neutron scattering experiments typically involve directing a beam of neutrons at a sample and measuring the momentum transfer of the neutrons that emerge from the sample. The intensity and distribution of the scattered neutrons provide information about the arrangement of atoms in the material, the presence of defects or impurities, and the motions of atoms and molecules within the material. Starting with the generation of a stream of neutrons, directing this stream through a sample, tracking the positions and times at which scattered neutrons interact with a detector and analyzing alterations in energy (E) and momentum (Q) exhibited by the scattered neutrons, the crystal structure of the material under investigation can be discerned.[22] Two approaches are employed to generate the neutron beams essential for scattering experiments. One method involves harnessing nuclear fission within a reactor, constituting a continuous source of neutrons.[23] Alternatively, neutrons are produced through spallation when accelerated protons collide with a heavy metal target, resulting in a

pulsed source of neutrons. The High Flux Isotope Reactor (HFIR) at the Oak Ridge National Laboratory (ORNL), which was used for this experiment is a reactor-based neutron source. In this chapter, an introduction to the neutron scattering techniques will be provided and the principles lying behind the triple axis spectroscopy setup for inelastic neutron scattering will also be discussed. [21,22]

2.2 Triple-axis neutron spectroscopy

Neutron facilities host a diverse array of specialized instruments tailored to accommodate a broad spectrum of experiments, each offering unique coverage Q and E transfers. The triple-axis spectroscopy and time-of-flight spectroscopy stand out as the most prevalent neutron scattering techniques. Notably, these spectrometers diverge in their methods for measuring energy transfer. The triple axis spectrometer at the HFIR beam room in HB3 setup was used for this experiment.

A layout of a triple-axis spectrometer is shown in Figure 2.1. Neutron beams, originating from the reactor, are initially filtered through a single crystal monochromator, selectively isolating neutrons with specific wavelengths (energies). Subsequently, this refined beam targets the sample under investigation. Upon interaction with the sample, scattered neutrons are redirected by Bragg reflection from the single crystal analyzer to determine their final energies. The analyzer utilizes Bragg scattering to

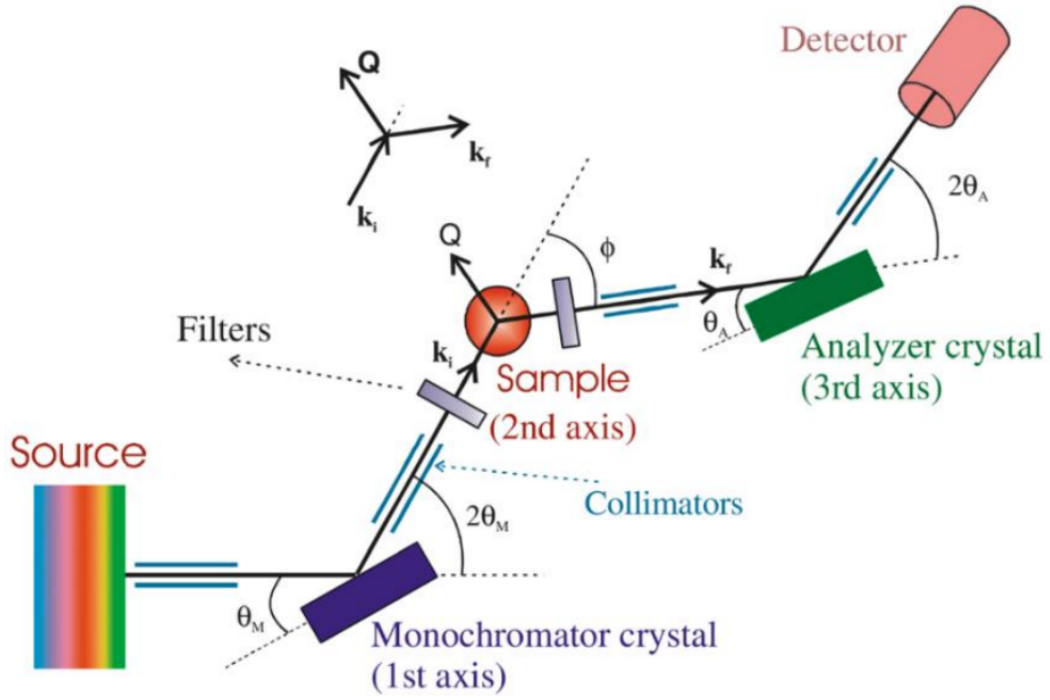

Figure 2.1: A schematic layout of a triple-axis neutron spectrometer. The figure is from Ref.[23].

further refine and select outgoing neutron energies. Ultimately, the neutrons reflected by the analyzer are captured by the neutron detector [24].

Within the framework of triple-axis neutron spectrometers, measurements involve collecting scattered intensity data at specific points within the momentum and energy transfer space. This spectrometer setup offers greater flexibility by allowing independent rotation of the sample (usually a single crystal), the monochromator, and the detector. This flexibility enables the study of intermediate-energy excitations, helps to clarify phase transitions, and provides insights into the structural characteristics of the material.[24].

2.3 Fundamentals of neutron scattering

During a scattering process, wherein a beam of neutrons or X-ray photons encounters the sample, the conservation of total energy and momentum is held. The momentum imparted from a neutron to the sample is defined as:

$$\vec{Q} = \vec{k} - \vec{k'} \tag{2.1}$$

where $\vec{k}$ and $\vec{k'}$ are the wavevectors of the incident and scattered beams respectively. The angle between $\vec{k}$ and $\vec{k'}$ is defined as 2θ.[14] Figure 2.2 gives the scattering geometry.

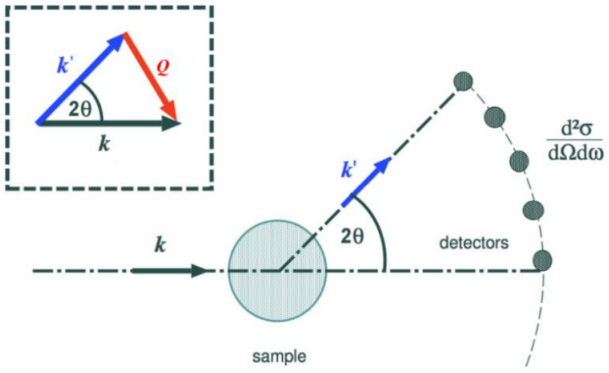

Figure 2.2: A schematic representation of the neutron scattering layout. $\vec{k}$ and $\vec{k'}$ are the wavevectors of the incident and scattered beams respectively. The angle between $\vec{k}$ and $\vec{k'}$ is defined as 2θ. The difference between $\vec{k}$ and $\vec{k'}$ is defined as $\vec{Q}$. Measurement of $\vec{k'}$ is used to calculate the momentum transfer. The figure is from Ref.[25].

The energy gained or lost by the beam can be expressed as:

$$dE = E - E' = \hbar\omega = \frac{\hbar^2}{2m}(|\vec{k}|^2 - |\vec{k'}|^2) \tag{2.2}$$

where $\hbar$ is the reduced Planck constant, ω is the angular frequency, and m is the mass of the neutron.[14] Analyzing the kinetic energy and momentum of both the incident and scattered beams facilitates the determination of the momentum transfer and the energy exchange experienced by the sample. This comprehensive examination yields valuable insights into the structural and vibrational characteristics of the material under investigation. During a neutron scattering experiment, the focus is measuring the double differential cross section $\frac{d^2\sigma}{d\Omega d\omega}$.[22] This quantity represents the number of neutrons scattered per second into a solid angle $d\Omega$, with energies falling within the range from $\hbar\omega$ to $\hbar(\omega + d\omega)$, and it's normalized by the incident neutron flux.

Neutron scattering experiments are commonly classified into two types, distinguished by the conservation or alteration of the neutron's kinetic energy throughout the process. These types are elastic and inelastic neutron scattering. Elastic neutron scattering primarily serves to discover the crystal structure of materials, whereas inelastic neutron scattering is predominantly employed to investigate excitations within the material.[22]

Bragg's law is an important principle used in neutron scattering. Bragg's law describes the relationship between the wavelength of X-rays or neutrons, the angle of

incidence, and the spacing between atomic planes in a crystal lattice.[26] It states that constructive interference occurs when the path difference between waves scattered by adjacent atomic planes is an integer multiple of the wavelength. Mathematically, it can be expressed as:

$$2d\sin(\theta) = n\lambda \tag{2.3}$$

where d is the spacing between atomic planes, θ is the angle of incidence, λ is the wavelength of the incident radiation, and n is an integer representing the order of the diffraction peak.[22] Figure 2.3 shows the schematic representation of Bragg's law conditions.

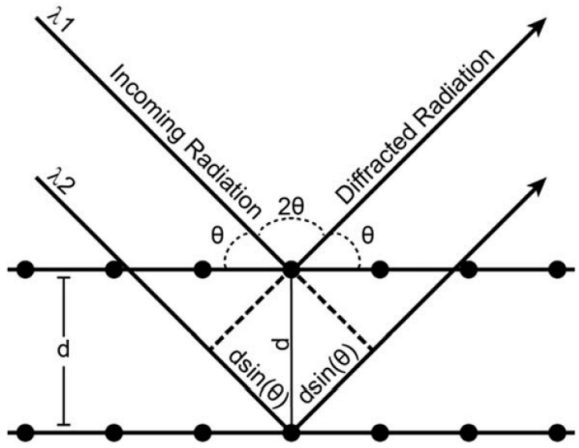

Figure 2.3: A schematic representation of Bragg's law conditions. λ_1 and λ_2 are wavelengths of two incoming radiations, which scatter off two atomic planes. The angle between the incoming and diffracted radiation is defined as 2θ. The displacement between two adjacent atomic layers is defined as d. When $2d\sin(\theta) = n\lambda$ condition is satisfied by a diffracted radiation, peaks are visible in the momentum space. The figure is from Ref.[26].

2.4 Uniaxial strain measurements

A change in the structural transition temperature was expected when pressure in applied in one of the three lattice directions a, b and c. The application of pressure and inelastic neutron scattering was conducted at ORNL in Tennessee, USA. A few tungsten (W) doped $MoTe_2$ samples (percentage of doping = 0.9%) were also tested.

2.4.1 Sample preparation

Some sizable $MoTe_2$ and MoW_xTe_{1-x} crystals were chosen and cut into 2 mm x 2 mm rectangular shaped cubic crystals using a USB microscope. A 0.5 mm x 0.5 mm mesh grid was laminated and was used to check if two interfacing sides of the crystal are parallel to each other. If the two parallel sides to which uniaxial pressure is applied are not exactly parallel, then the crystal tends to bend and buckle along any discrepancies along the layers, failing to withhold pressure and eventually failing the experiment.

2.4.2 Sample alignment

Located at the CG-1B port within the HFIR Guide Hall, the alignment diffractometer facilitates sample alignment and component testing. Samples are typically affixed to a goniometer equipped with motorized 2-axis tilt and translation capabilities. Detection of Bragg peaks is achieved using a single 3He detector. Figure 2.4 shows a mounted sample at the alignment station.

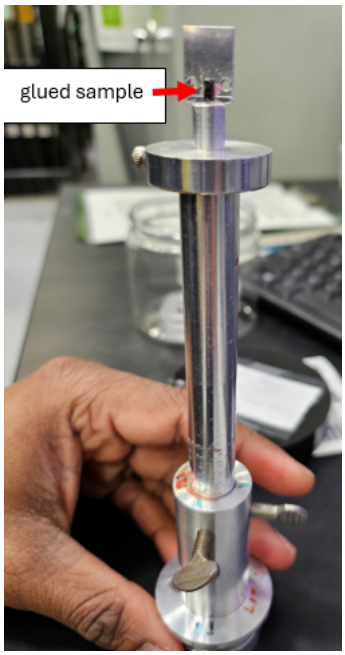

Figure 2.4: Sample mounting to the stick at the alignment station. A $MoTe_2$ crystal is glued on the top side surface of the sample mounting stick and was exposed to the neutron beam to find the correct a, b and c directions.

Each sample was mounted into the stick with the use of Loctite 4503 instant adhesive glue, by taking the direction which needs to be observed into consideration. The goal of sample alignment was to check for available Bragg peaks with the relative intensities as well as to identify the tilts of the samples if any. Goniometer can only move a maximum of 6° to either side when the cryostat is loaded at HB3, so finding the crystals with a lower tilt and better crystalinity (sharp Bragg peaks) was necessary. 002 and 201 peaks were observed for each and every sample and the tilt was also recorded. The samples were heated above room temperature to ensure that they are at the monoclinic phase before loading to the triple axis spectrometer.

Figure 2.5: Sample alignment station setup

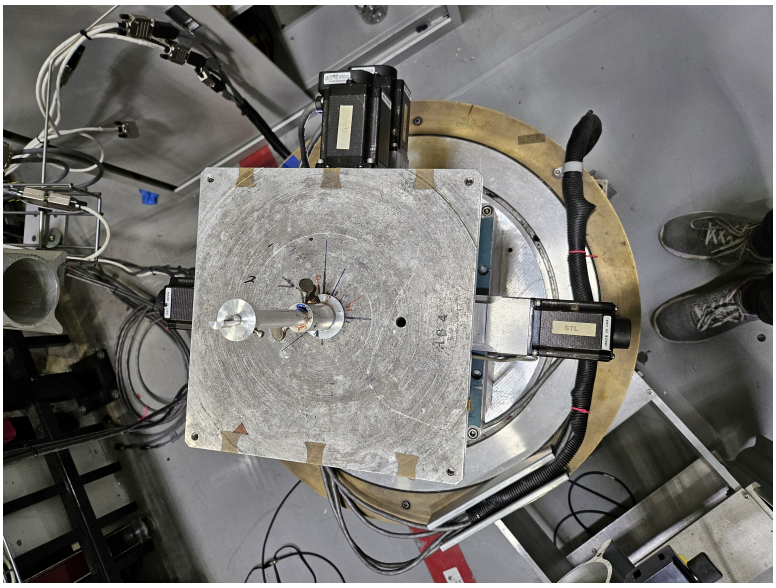

Figure 2.6: Sample alignment table

2.4.3 Sample loading

The uniaxial pressure cell developed by the Pengcheng Dai group was used to conduct the experiment. First, the dimensions of the samples were measured to calculate the applied pressure from the area of the sample and the applied force. The distance from the top of the stick to the middle of the pressure chamber was measured to find out the sample positioning information and spaces made of aluminum (Al) were used to fit the sample in the pressure cell at the desired height. The orange cryostat could reach a base temperature of 1.8 K with a maximum temperature of 311 K. To load the sample, the pressure cell chamber was taken out and the sample was fixed to a spacer using loctite glue under a light-microscope. Then the spacer with the sample was fit into the rest of the pressure cell and some pressure was applied from the two stainless steel screws at the bottom with the help of another spacer on top. The bottom part of the pressure cell was covered with gadolinium oxide paper to avoid the appearance of Bragg peaks due to Al or copper (Cu) from the alloy in the screws. A temperature sensor was also connected to the inside of the pressure chamber as the temperature of the sample lags behind the real time temperature. Then 'UniaxGen3', which is the interface which deals with the application of pressure, to see if there is actually movement of the pistons to apply pressure. The pistons can move in units of 0.03 mm, 0.10 mm or 0.50 mm. After checking the offline performance, the stick was inserted to the orange Cryostat. Uniaxial strain can be applied vertically, perpendicular to the

scattering plane for measurement. Figure 2.7 shows the loaded sample in the pressure cell chamber under a light microscope and Figure 2.8 shows the loaded pressure cell to the stick.

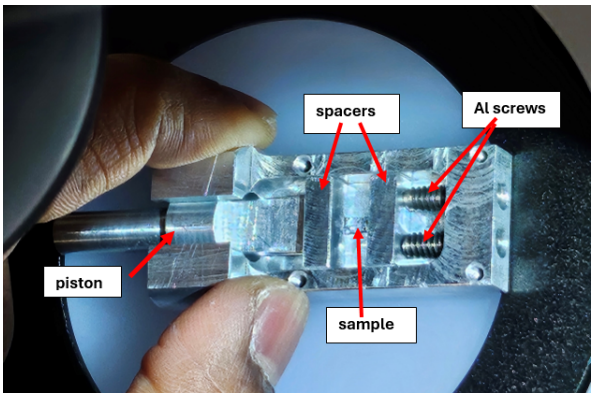

Figure 2.7: Sample loading to the mechanical pressure cell. Sample was carefully placed between two spacers and fitted into the pressure cell. Al screws at the bottom of the cell was tighned and the piston on the top of the cell was moved until it barely touches the top spacer.

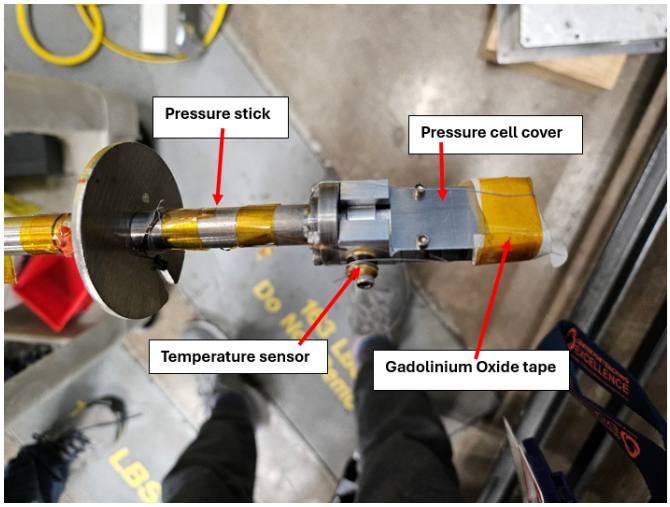

Figure 2.8: Pressure cell loading to the pressure stick. Pressure cell was secured by its cover and attached to the end of the stick. The temperature sensor was attached to record the temperature of the sample. Bottom part of the pressure cell was covered with gadolinium oxide tape to prevent neutron scattering peaks rising from the Al screws at the bottom.

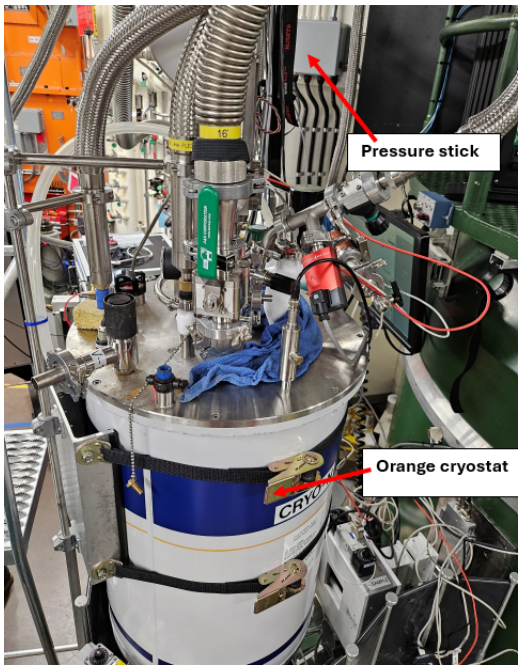

Figure 2.9: Pressure stick on top of the orange cryostat. Pressure cell was loaded into the orange cryostat by inserting the pressure stick.

Uniaxial strain measurements along the a or b direction, a pivotal consideration lies in ensuring the perfect parallelism of the cubical crystal's sides. Any deviation from complete parallelism, even by a minute margin, poses a critical challenge. Conventional tools like diamond grade sandpapers or wire saws, typically employed for crystal cutting, cannot guarantee the requisite precision due to the inherent risk of inducing layer sliding during the preparation process. Given the weak inter-layer coupling inherent in $MoTe_2$, this risk is particularly pronounced. An observational study during the conducted inelastic neutron scattering experiment underscored this challenge,

manifesting in the bending and buckling of crystals across almost inevitable defective grain boundaries. Experimental protocols involved the application of pressure in translational steps of 0.03 mm, monitored using the UniaxGen3 software interface. Any indication of buckling necessitated immediate intervention, as failure of the uniaxial pressure setup was imminent. The unloading and reloading of samples, a labor-intensive process exacerbated by the weight of the Orange cryostat, consumed over 8 hours per cycle, limiting throughout within the experimental time-frame. Attempts with smaller samples yielded negligible Bragg peak intensities against background noise, with samples succumbing to buckling prior to the reaching a pressure of 1 MPa.

When it was realized that application of pressure in one of the in plane directions are impossible with the given resources and setup, there was no choice but to move to the out of plane c-axis direction for the application of uniaxial pressure. $MoTe_2$ crystals for uniaxial pressure along the c-direction offline, prior to exposure to the neutron beam. Encouragingly, the results revealed stable pressure retention over 18 pressure steps, each involving a piston translation of 0.03 mm.

Initially, the 002 in-plane peak, characterized by its high intensity, was located. Subsequently, the tilt was scanned to ensure it remained below 6 degrees. Once the sample was aligned with the maximum tilt, the slits were systematically adjusted to optimize intensity. A temperature scan was conducted overnight to determine the sample's transition temperature prior to applying pressure. This initial temperature

dependence run served as the control throughout the subsequent pressure experiments on this particular sample. As pressure was incrementally applied, the resolution of peaks at room temperature was observed. In W-doped samples, completion of one temperature hysteresis loop and return to room temperature typically resulted in a mixed state of both monoclinic and orthorhombic phases. Typically, in order to resolve these two phases and to make the sample fully transition into the monoclinic phase, temperature should be increased above 320 K. The application of pressure revealed the clear resolution of monoclinic and orthorhombic peaks at room temperature for the W doped $MoTe_2$ samples, indicating a reduction in the transition temperature. Continuation of this process eventually led to a pressure at which the sample entirely transitioned to the monoclinic phase at room temperature.

Chapter 3

Synthesis and characterization

3.1 Flux growth of $MoTe_2$

$MoTe_2$ single crystals were synthesized using the flux growth method: Mo and Te powders were mixed together in a 1:2 molar ratio and pressed into a pellet. Enough excess Te was added so that the mass ratio of the $MoTe_2$ pellet to the Te flux was 1:3. The parts were then sealed in an argon-filled fused quartz glass ampoule, which was then heated up to 1150 °C and slowly cooled down to 950 °C over the span of about 3 weeks. At 950 °C, the ampoule was quenched in water or liquid nitrogen to trap the monoclinic phase at room temperature. The $MoTe_2$ crystals formed are covered in Te flux. At this point, an extra step of post-annealing was done by sealing the product inside another quartz ampoule heating up to 1000 °C, just above the melting temperature of Te. At 1000 °C, Te becomes a liquid, while the $MoTe_2$ crystals remain solid. This method was used to remove excess Te from the $MoTe_2$ crystals. Figure 3.1 shows the positioning of the quartz ampoule inside the 2-zone furnace for optimum crystal growth. Figure 3.2 shows an example of a grown $MoTe_2$ crystal.

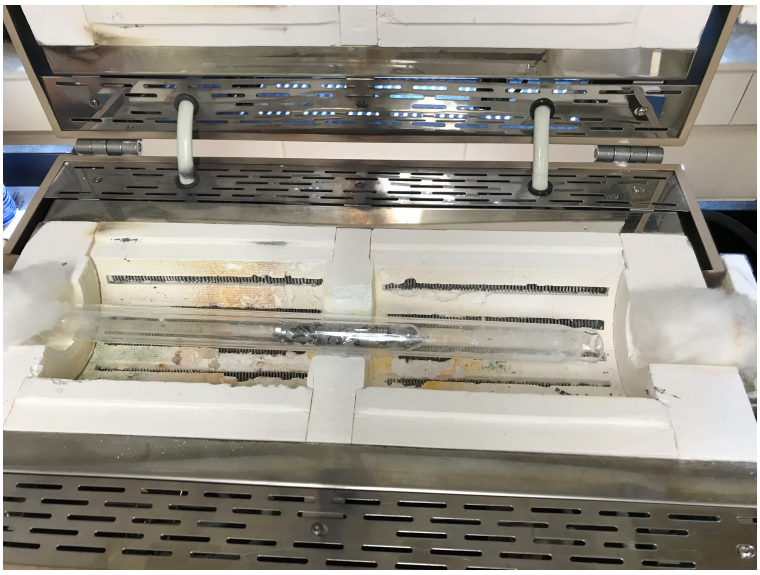

Figure 3.1: Positioning of the ampoule inside the 2-zone furnace to maximize the crystal yield. A temperature gradient of 50 °C was maintained between the two zones of the furnace and the opening ends of the chamber was closed with quartz wool to minimize heat drainage.

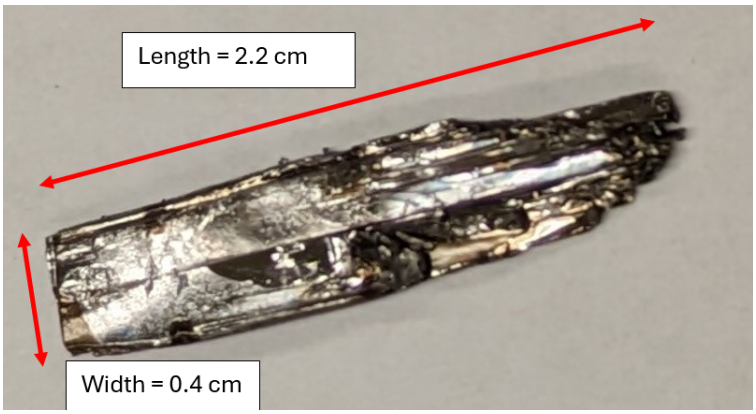

Figure 3.2: An example of a monoclinic $MoTe_2$ crystal. a axis is along the width and b axis is along the length. Clear layer like crystal grwoth can be seen along b axis.

Some materials melt congruently (where the compound decomposes so that the liquid is the same composition as the compound), but many materials melt incongruently. If $MoTe_2$ is heated up, it would decompose to liquid Te and Mo_3Te_4. $MoTe_2$ can still

be crystallized using excess Te. There are a few different ways to grow crystals. The flux growth method is a technique for growing crystals in which the initial materials are dissolved in a solvent (flux) and then precipitated to form crystals of the desired compound. The flux reduces the melting point of the target compound, similar to the process of recrystallization in wet chemistry.[11] In this case, Te (melting point 850 °C) is part of $MoTe_2$, which is named as self flux growth.[11] Other liquids can also be used for the purpose of growing crystals in general. If water is used, it's called solution growth. If a powder of the material is needed instead of the single crystals, then solid-state reaction synthesis technique can be used. The exact stoichiometric ratio of the ingredients at a low temperature will then be used, lower than the melting temperature of the materials.[10] This is often called sintering. $MoTe_2$ can also be made by a chemical vapor transport technique, where a small amount of iodine is added and the transport occurs between the hot and cold ends of an ampoule. [27]

3.2 Transport characterization

The PPMS was used for transport measurements of $MoTe_2$ crystals. A sizable $MoTe_2$ crystal was cut into a rectangular shape. A resistivity puck with 3 channels and 4 terminals for each channel (I+, I-, V+, V-) was chosen. Leads I+ and I- were for current, and the leads V+ and V- were for voltage. To attach the crystal to one of the channels, silver paint, Platinum (Pt) wires, and epoxy glue were used. If in-plane (a or b axis) resistivity measurements were needed, then the sample was glued with

the stacking direction along the vertical axis to be perpendicular to the horizontal surface of the puck.

To attach a sample to the puck, first, the copper (Cu) conducting surface of the puck was cleaned thoroughly with a Q-tip dipped in ethanol. A cigarette paper piece was cut to fit the open area of the Cu surface, and it was then glued to the Cu surface using epoxy glue. The sample was taken under a light microscope, and 4 Pt wires were placed at even distances along the in-plane direction, and the connections were secured with fast-drying silver paint. The connected crystal was put on top of the puck closer to the desired channel, and a bit of epoxy glue was used to secure the sample to the puck. The other ends of the Pt wires were then reconnected to the four terminals of the channel using solder. With the sample now securely connected to the puck and wired to the terminals, a bridge setup was used to see if non-fluctuating resistance values were displayed between each two connections. Passing this test, the puck was ready to be loaded into the PPMS.

The resistivity puck was loaded into the PPMS chamber. A script was written to measure the resistance of the sample during every chosen time frame for a desired period of time. A plot of the change in resistance of the sample with the change in the temperature was plotted, with temperature rising up to 350 K from room temperature, followed by cooling down to 2 K, then rising back up to 350 K. The obtained temperature dependent resistance curves are discussed in the results section.

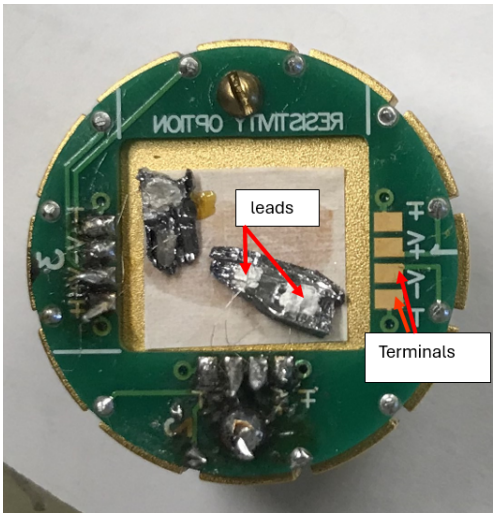

Figure 3.3: A resistivity puck with samples loaded. Two $MoTe_2$ crystals are connected to terminals 2 and 3 for out of plane transport measurements.

For transport measurements along the c axis (layer stacking direction), two Pt wire connections are made to each in-plane surface of the cuboid shaped crystal under a light microscope and the sample was glued vertically to the puck. The connections to the terminals from the leads can be made such that the path of the current through the c-axis of the crystal is direct or indirect (crossover). There are three methods that c-axis transport measurements can be performed. Two leads can be connected to each inplane surface of the crystal in all three cases. The variation of the methods comes with the horizontal/vertical placement of the in-plane surfaces of the crystal and the connection pattern of the leads to the terminals. Method one is when the crystal is glued to the puck through the inplane surface. The problem with this method is that the glue can get in the way of the connection of the leads, giving erroneous results in the resistivity measurements.Figure 3.3 shows an example of a resistivity puck made

by method 1. The second and third methods involve positioning the crystal vertically, making the c-axis parallel to the direction of connection of leads. Method 2 is when the current and voltage leads were facing the respective counter lead (I+ facing I- and V+ facing V-) and have direct pathway to get through the crystal. Method 3 is when the current and voltage leads were interchanged on either side of the crystal, making the current go through a longer path through the crystal. Figure 3.4 shows the different methods to connect leads to a $MoTe_2$ crystal for out-of-plane transport measurements.

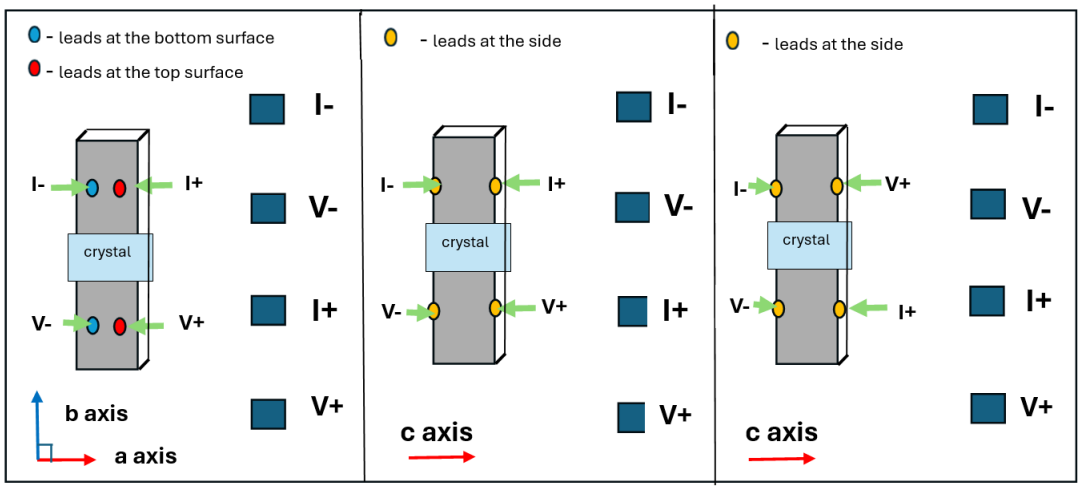

Figure 3.4: Different methods to connect leads to a $MoTe_2$ crystal for out-of-plane transport measurements: left - method 1, middle - method 2, right - method 3.

Chapter 4

Transport results

4.1 Inplane transport

The temperature dependence of in-plane electrical resistivity measurements on a single crystal of $MoTe_2$ down to T_{min} = 2.0 K at ambient pressure is shown in Fig. 4.1. The resistivity exhibits metallic behavior with a thermal hysteresis setting in below room temperature. Two hysteresis curves can be seen in Fig. 4.1, one between 2 - 300 K and the other between 200 - 300 K. The thermal hysteresis loops in the temperature range of 200 - 270 K can be observed due to the first order structural phase transition taking place when the crystal system moves from monoclinic to low temperature orthohombic. During this phase transition the atomic layers are sliding on top of each other, until they perfectly align to be placed into orthorhombic upon cooling or monoclinic upon warming. Fig. 4.1 is consistent with the previously observed electrical resistivity behavior in $MoTe_2$. [18]

The residual resistivity (RR) of a sample is defined as the resistivity at T_{min}, which in this case is 2.0 K.[12] It reflects the presence of defects or other localization effects the electrons experience at low temperatures. A RR of about 3.6 $\mu\Omega$ m was observed at

zero field. Below 0.2 K, at about 0.1 K, the superconducting transition temperature T_c can be reached, where a sudden drop in the resistivity curve is observed. [18] Such measurements were not possible with our existing system.

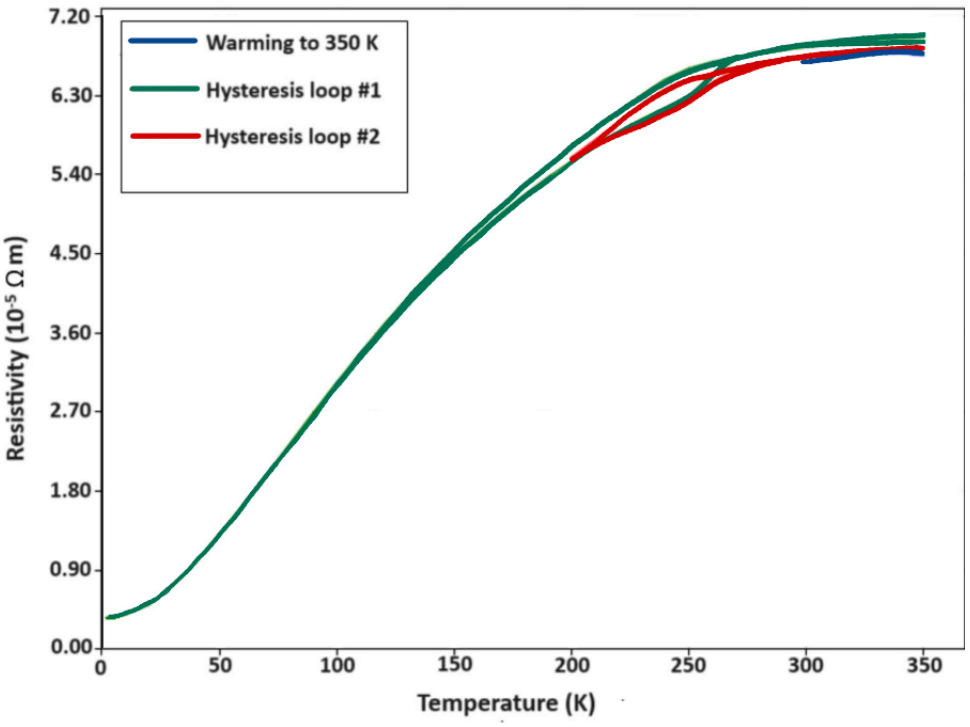

Figure 4.1: Inplane resistivity vs. temperature curves of $MoTe_2$ at ambient pressure. The blue curves represents warming upto 350 K from the room temperature. The green curve represents cooling down to 2 K and warming up to 350 K again. The red curve represents cooling to 200 K and warming up to 350 K. Temperature hysteresis curve is present between 200 - 270 K, during which layer sliding and diffuse scattering takes place to rearrange the crystal structure to high temperature monoclinic or low temperature orthohombic.

4.2 Out of plane transport

Out of plane transport was measured to observe the change in the hysteresis loop with any effects from layer stacking disorder. No previous studies have been conducted to see the resistivity variance in the out of plane direction in $MoTe_2$. An interesting behavior occurred repeatedly in many out of plane transport trials. As previously discussed in the characterization of $MoTe_2$, 3 methods were used. One important observation for all of the observed plots is the hysteresis loop does not close up to 350 K. In inplane measurements the hysteresis loop is completed at 300 K, forming a closed loop. But, along the c-axis, the hysteresis loop stays open within the measured range of 200 - 350 K, as can be seen from multiple trials. Fig. 4.2 shows the resistivity vs. temperature curve for method 1. The sample was warmed up to 350 K and then cooled down to 2 K. Upon warming back up, the hysteresis loop does not close up to the measured maximum temperature of 350 K. The same trait can be observed in Fig. 4.3, which shows the resistivity vs. temperature curve for method 2. The sample was warmed up to 350 K, then cooled down to 2 K, and warmed back to 350 K. The hysteresis loop remains open until 350 K. Fig. 4.4, which shows the result for method 3, also shows the same behavior, as the temperature hysteresis loop remains open up to 350 K.

From the neutron scattering measurements, it was earlier observed that diffuse scattering emerges on the transition upon cooling from 1T′ to T_d [12]. This diffuse scat-

tering manifests itself into the T_d^* phase upon warming. The reason for these is due to the sliding of the atomic layers. When out of plane resistivity is measured, this layer sliding becomes prominent. Along the direction of vdW layers, monoclinic and orthorhombic phases coexist within the same crystal in different regions, making the hysteresis loop to be open ended until 350 K. Depending on the sample, if the structural transition temperature is lower, there is a chance for the resistivity loop to close before the temperature reaches 350 K. The variation in samples with regards to the structural transition temperature makes the closing of the hysteresis loop a variable as a function of the temperature.

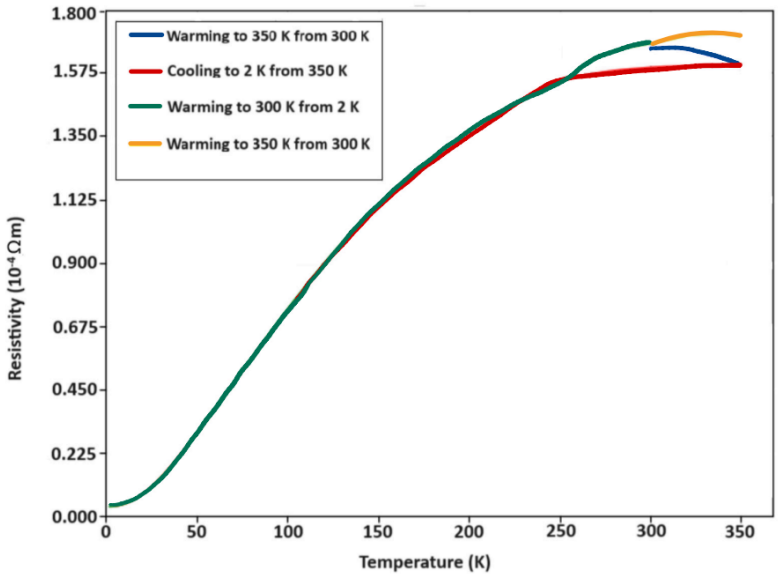

Figure 4.2: c-axis resistance vs. temperature curve of $MoTe_2$ at ambient pressure for method 1. The blue curve presents warming up to 350 K. The red curve represents cooling down to 2 K and the green curve represents warming up to 300 K. The yellow curve represents warming to 350 K from 300 K. The hysteresis loop opened at about 150 K has not closed at 300 K due to sliding of the layers.

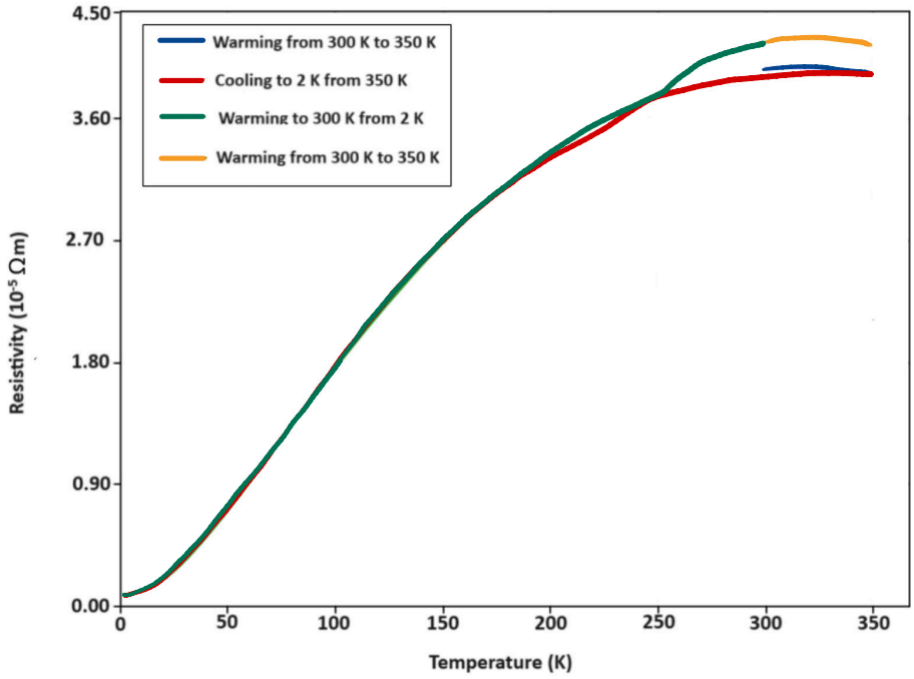

Figure 4.3: c-axis Resistivity curve of $MoTe_2$ at ambient pressure for method 2. The blue curve presents warming up to 350 K. The red curve represents cooling down to 2 K and the green curve represents warming up to 300 K. The yellow curve represents warming to 350 K from 300 K. The hysteresis loop opened at about 150 K has not closed at 300 K due to sliding of the layers.

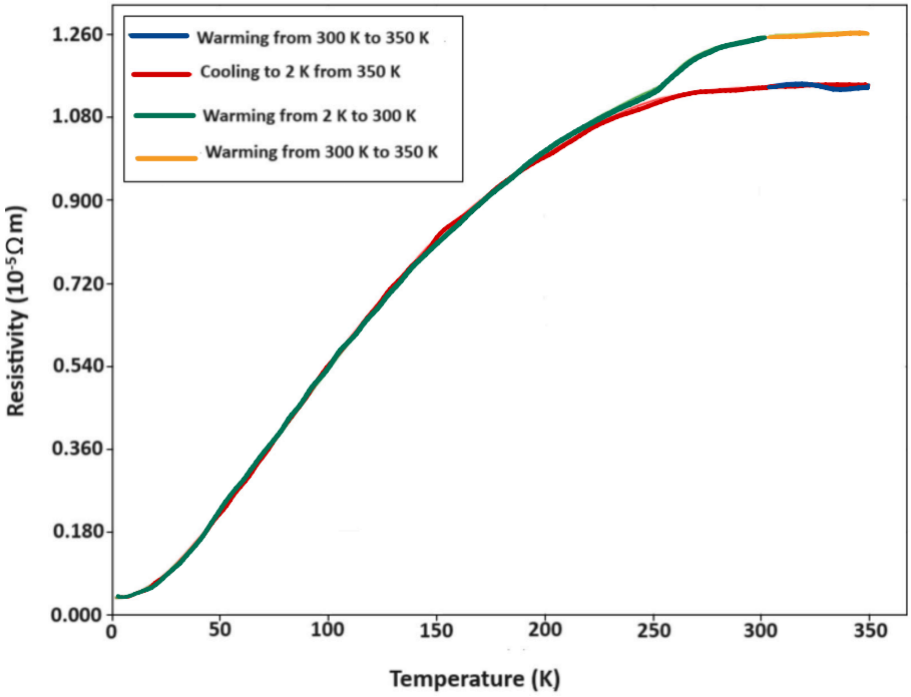

Figure 4.4: c-axis Resistivity curve of $MoTe_2$ at ambient pressure for method 3. The blue curve presents warming up to 350 K. The red curve represents cooling down to 2 K and the green curve represents warming up to 300 K. The yellow curve represents warming to 350 K from 300 K. The hysteresis loop opened at about 150 K has not closed at 300 K due to sliding of the layers.

Chapter 5

Neutron scattering under strain

5.1 In-plane uniaxial strain

Samples were subjected to neutron scattering while applying uniaxial pressure along a or b directions, to observe the changes in the structural transition temperature from monoclinic to low temperature orthorhombic. Trials in which uniaxial pressure was applied in either a or b direction failed due to bending and/or buckling of the samples along the prominent grain boundaries before even 1 MPa of pressure was reached due to the delicate nature of the stacked layers. Figure 5.1 shows the schematic of the crystal structure of 1T′ $MoTe_2$. Uniaxial pressure was applied in a or b direction for inplane measurements and along c axis for out of plane measurements in the layer stackign direction. Figure 5.2 shows two such buckled $MoTe_2$ crystals.

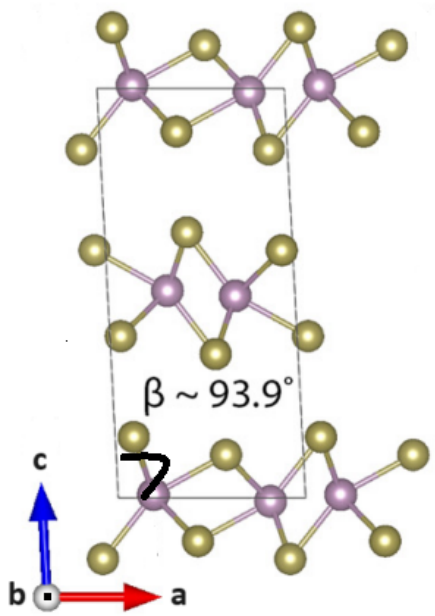

Figure 5.1: schematic of the crystal structure of 1T′ $MoTe_2$. Uniaxial pressure was applied in a or b directions for inplane uniaxial strain and in c direction for out of plane uniaxial strain measurements.

Figure 5.2: Buckled $MoTe_2$ crystals after application of uniaxial pressure along a or b directions. The buckling took place before a pressure of 1 MPa was applied.

5.2 Out-of-plane uniaxial strain

Out of plane uniaxial strain measurements were conducted to investigate the structural changes that occur under strain. The pressure was applied in the range of 0.1 - 13.5 MPa along the c axis. Figure 5.3 shows the pressure dependence of the peaks during the cooling process. At 300 K, the $20\bar{1}$ and 201 out of plane monoclinic peaks are visible, but when the temperature is lowered down to 230 K, the sample is fully transitioned to the T_{d} phase with the 201 T_{d} orthorhombic peak becoming visible. At ambient pressure, the structural transition happens around 245 - 250 K as can be seen in Figure 5.3. The temperature hysteresis was conducted in temperature steps of 10 K.

A 9% W doped $MoTe_2$ crystal with a stoichiometry of $Mo_{0.91}W_{0.09}Te_2$ was used to investigate the effect of uniaxial pressure along the c axis on the structural transition temperature. The black curve in Figure 5.4 shows the temperature dependent hysteresis at ambient pressure, from which it is evident that $20\bar{1}$, 201 monoclinic peaks as well as 201 orthorhombic peak is visible at 309 K. Therefore,it is clear that the used $Mo_{0.91}W_{0.09}Te_2$ sample was in a mixed state of monoclinic and orthorhombic phases at 309 K after the initial temperature hysteresis. The sample had not fully transitioned into the high temperature monoclinic phase at 309 K. Upon applying uniaxial pressure along c direction, as shown in Figure 5.4, the structural phase tran-

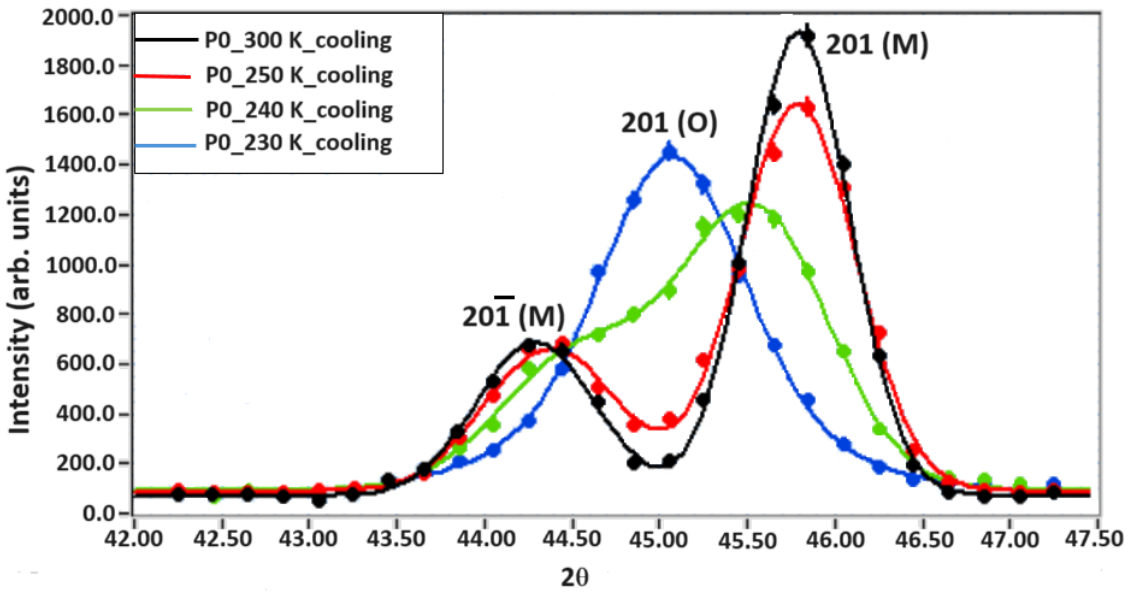

Figure 5.3: Structural phase transition from Monoclinic to low temperature orthohombic at ambient pressure for the $Mo_{0.91}W_{0.09}Te_2$ sample. At 250 K, sample is in the monoclinic phase, $20\bar{1}$ and 201 monoclinic peaks are visible. At 230 K, sample is in the orthorhombic phase, 201 orthorhombic peak is visible. Diffuse scattering takes place in the phase transition region. A narrow structural phase transition region can be identified between 240 - 245 K. (M) indicates a monoclinic peak and (O) indicates an orthorhombic peak.

sition is completed, by fully transitioning into the monoclinic phase under a pressure of 2.5 MPa. Uniaxial pressure along the c direction has promoted the transition to the monoclinic phase from a mixed state of monoclinic and orthohombic phases at 309 K. Hence, it can be argued that uniaxial pressure along the c direction promotes layer sliding to properly transform into the 1T′ phase. At ambient pressures to reach the monoclinic phase for the tested $Mo_{0.91}W_{0.09}Te_2$ sample a temperature above 310 K should be achieved. But, with the application of uniaxial pressure along the c direction, the monoclinic phase can now be reached at 309 K with a pressure of 2.5 MPa. The diffuse scattering is also significantly suppressed.

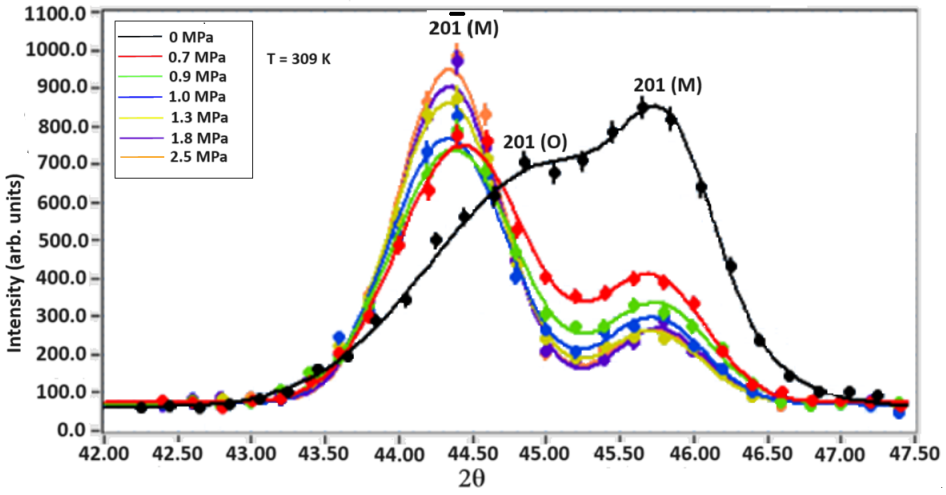

Figure 5.4: Change in the peak intensities with applied pressure at 309 K (fixed temperature) for pressures 0 - 2.5 MPa for the $Mo_{0.91}W_{0.09}Te_2$ sample. It is evident that the $20\bar{1}$ and 201 1T′ peak intensities are increasing and the 201 T_d peak intensity is lowering, which provides for the fact that the monoclinic peak is getting prominent ahead of the orthohombic peak. This means that the transition temperature should be lowered until 2.5 MPa. (M) indicates a monoclinic peak and (O) indicates an orthorhombic peak.

When the pressure is further increased upto 13.5 MPa, the sample fully transitions to the monoclinic phase, which can be seen from Figure 5.5. The intensities of the $20\bar{1}$ and 201 1T′ peaks increase with the application of uniaxial pressure, indicating the increasing dominance of the monoclinic phase.

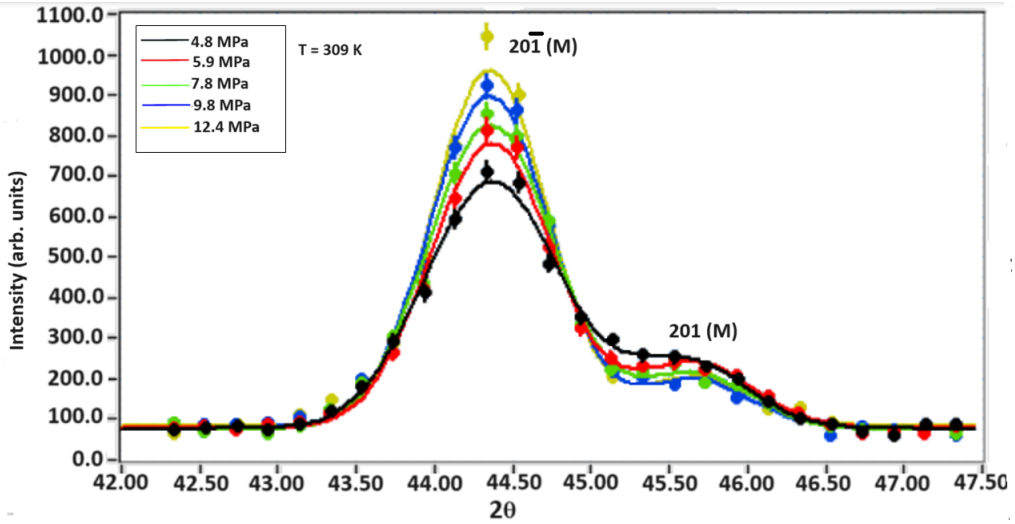

Figure 5.5: Change in the peak intensities with applied pressure at 309 K (fixed temperature) for pressures 4.8 - 13.5 MPa for the $Mo_{0.91}W_{0.09}Te_2$ sample. It is evident that the $20\bar{1}$ and 201 1T′ peak intensities are increasing, which provides for the fact that the monoclinic peak is getting prominent with increasing pressure. This means that the transition temperature should be lowered until 13.5 MPa. (M) indicates a monoclinic peak.

Chapter 6

Discussion

The first order structural phase transition from monoclinic to low temperature orthorhombic in $MoTe_2$ was studied with transport and elastic neutron scattering. The in-plane transport results agree with previously reported results [18], exhibiting metallic behavior with a long tailed thermal hysteresis curve settling below room temperature. The phase transition from monoclinic to low temperature orthorhombic can be identified from the sudden increase in the gradient of the temperature dependent resistivity curve within the range of 250 - 270 K, the exact transition temperature explicitly dependent on the layer stacking of each individual crystal. The inplane temperature dependent resistivity curves always form closed loops below room temperature, indicating a narrow temperature region within which the structural transition is completed, with perfect assembly of atomic layers to give rise to low temperature orthohombic structures. The hysteresis in the resistivity and the diffuse scattering from the earlier neutron scans signal variations in the occurrence of 1T′ and T_d twin boundaries. The hysteresis loop is associated with the first order structural transition and is a wide open loop until 350 K in out-of-plane transport. This accounts for the fact that in the layer stacking direction, layer sliding occurs during the structural

transition, which gives rise to monoclinc and orthorhombic phase regions coexisting at a same temperature. Hence, the hysteresis loop remains open until 350 K. This is mainly due to the sliding of atomic layers, which is evident when out of plane resistivity is measured. If the structural transition temperature were lower, the resistivity loop may have closed before reaching 350 K. Variations in structural transition temperatures among samples cause the hysteresis loop to close at different temperatures. The layer stacking disorders hinder the completion of the layer sliding in a narrow temperature region, which is evident from the c axis transport measurements.

Application of uniaxial pressure in the layer stacking direction promotes the layer sliding, hence narrowing the phase transition temperature region and suppressing the diffuse scattering. Neutron scattering measurements along 0kl has shown diffuse scattering streaks and along hol, little to no diffuse scattering has been observed. [11] There should not be any diffuse scattering in the hk0 plane. Figure 6.2 shows the neutron scattering intensity maps along h0l and 0kl planes. Previously reported structural phase transition temperature of 270 K of $Mo_{0.91}W_{0.09}Te_2$ [12] was lowered to 245 K with the application of uniaxial strain in the layer stacking direction. Hydrostatic pressure has been shown to decrease the transition temperature [12]. Tensile strain along the a or b axes has been reported to, respectively, decrease and increase the transition temperature [17]. The effect of non-hydrostatic stresses on $MoTe_2$, however, has not been studied with diffraction techniques before, and the question of how a uniaxial stress along the c-axis would affect structural properties has now

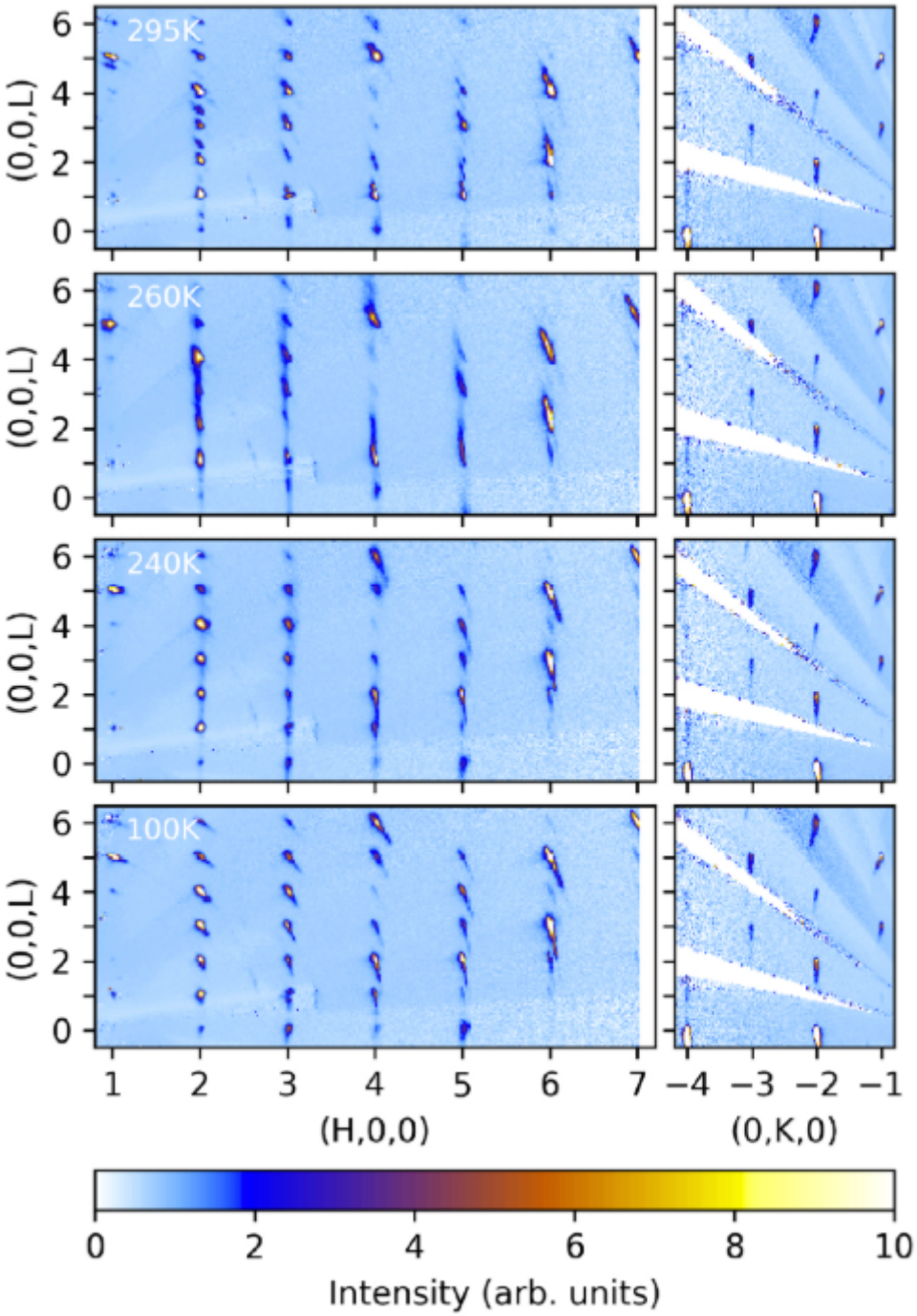

Figure 6.1: Neutron scattering intensity maps of the H0L and 0KL planes. Diffuse scattering streaks appear along L in the H0L plane only, upon cooling from 295 to 240 K. By comparison, in the 0KL plane, no diffuse streaks are observed. This figure was taken from [11].

been answered. $MoTe_2$ is much more compressible along the c axis than along the a or b axes, increasing the number of interlayer interactions, promoting layer sliding along a narrower temperature region to complete the structural transition. However, unlike in the case of application of hydrostatic pressure, there is a limitation of the application of uniaxial strain along the c axis, as the increment of pressure with each successive uniaxial translation becomes saturated above 13.5 MPa.

Figure 6.2 shows the temperature dependent peak intensities of the projections of the $20\overline{1}$, 201 1T′ and 200, 201 T_d peaks on the c axis. Upon increasing the strain from 0 to 0.5 MPa, the intensity of the projections of the $20\overline{1}$ and 201 1T′ peaks switch, making the $20\overline{1}$ peak projection dominant. Upon the further application of pressure upto 13.5 MPa, the intensity of the $20\overline{1}$ 1T′ peak projection increases while that of the 201 peak intensity decreases. This can be explained using the argument of the presence of two polar domains in $MoTe_2$ structures which defer by the β angle between the b and c axes [32]. These two domains have β angles of 93.91° and 86.12°. Upon the application of uniaxial pressure, it is possible that the structure changes from one polar domain to the other, making one domain entirely dominant over the other upon a threshold value of uniaxial pressure. Further experimentation is needed to validate this theory and if the domain changing really happens with the application of uniaxial pressure, this may open new avenues in the area of domain engineering.

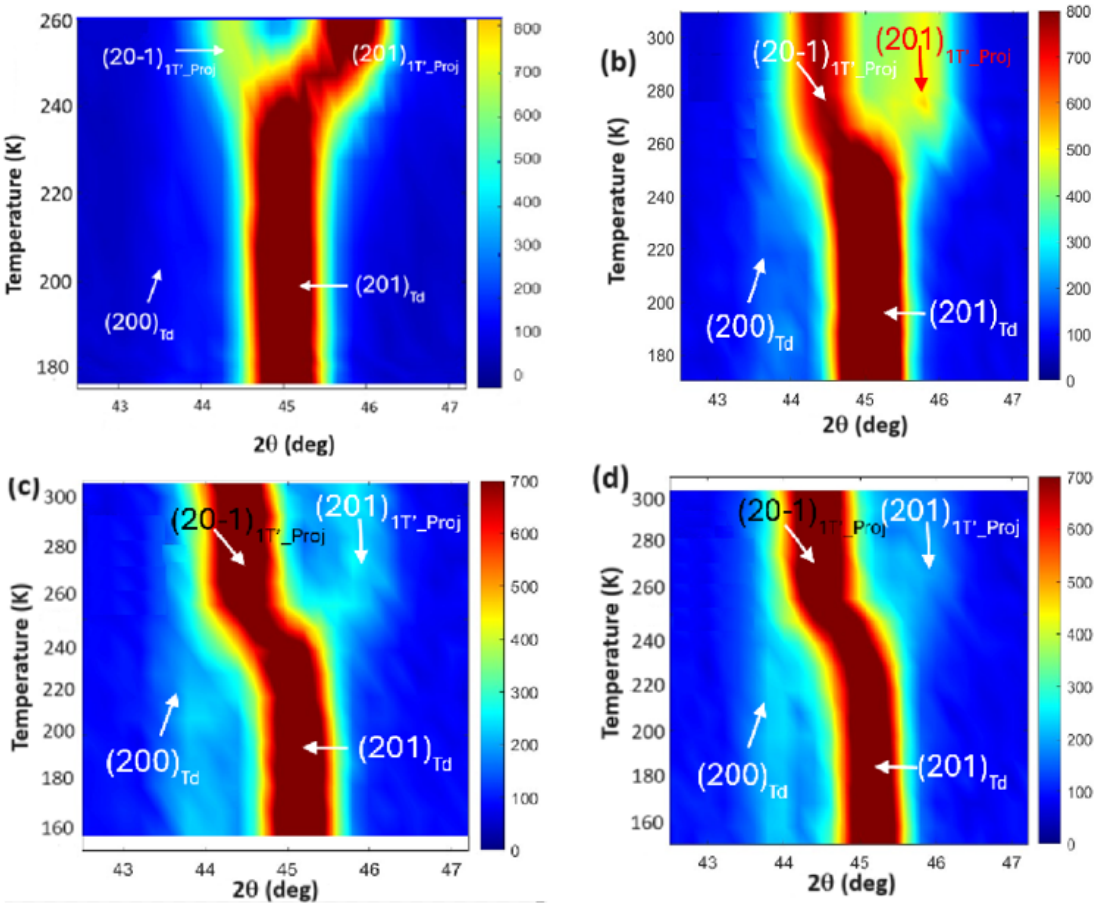

Figure 6.2: Temperature dependent peak intensity diagrams for four pressure values upon cooling (a) zero applied pressure, the projection of $20\bar{1}$ 1T′ peak on the c axis is relatively less intense than the projection of 201 1T′ peak on the c axis (b) 0.5 MPa applied pressure, the intensity of the $20\bar{1}$ 1T′ projection becomes more intense than that of the 201 1T′ peak projection (c) 2.5 MPa applied pressure, the intensity of the $20\bar{1}$ 1T′ projection increases in intensity while 201 1T′ projection decreases in intensity (d) 13.5 MPa applied pressure, the intensity of the $20\bar{1}$ 1T′ projection further increases in intensity while 201 1T′ projection further decreases in intensity.

Chapter 7

Conclusion

Topological Weyl semimetals are a class of innovative quantum materials featuring bulk Weyl fermions linked by topological surface Fermi arcs. $MoTe_2$ stands out among these materials due to its 2D layered structure, which holds significant promise for various applications. $MoTe_2$ exhibits high electron mobility and large MR, making it suitable for use in high-speed electronics and spintronics. To gain a deeper understanding of the Weyl physics in $MoTe_2$, it is essential to comprehend its crystal structure, as the emergence of Weyl fermions requires the breaking of inversion symmetry.

The structural phase transition in $MoTe_2$ was investigated using transport and neutron scattering under strain to reveal the effect of layer sliding and stacking disorders particularly in the c direction. The inplane transport resulted in a closed thermal hysteresis loop below room temperature with a rapid increase of the gradient during the structural transition range. The out-of-plane transport resulted in a broad hysteresis loop which remained open until 350 K. Upon warming, layer sliding occurring in the vdW layer stacking direction opens regions of transitioned monoclinic and not yet transitioned orthorhombic phases, which can be the reason for the hysteresis loop to

stay opened up to 350 K. The sliding of layers along which should be perfectly aligned to give rise to the high temperature monoclinic and low temperature orthorhombic structures along with the defects in layer stacking have been identified as the probable cause for the discrepancy between the in plane and the out of plane transport results. Application of uniaxial pressure along the layer stacking direction of a $Mo_{0.91}W_{0.09}Te_2$ promoted the monoclinc phase over the mixed state of monoclinc and orthorhombic phases at T = 309 K up to a strain of 13.5 MPa. The applied uniaxial pressure started to saturate after 13.5 MPa, above which it was impossible to further increase the strain along the c axis of a $Mo_{0.91}W_{0.09}Te_2$ crystal. It was evident that uniaxial pressure along the c direction supresses the diffuse scattering within the structural transition region, promoting the sliding of the layers. Transport without strain showed that the structural transition temperature range became wider because of the sliding of the layers. But, diffuse scattering increases under strain, meaning the layers slide back and forth rapidly than in the case of without strain, contrasting the hypothesis of suppression of the layers with strain. The abrupt change in the peak intensities of the $20\bar{1}$ and 201 1T$'$ peak projections along the c axis upon application of uniaxial pressure indicated signs of one polar domain becoming more prominent over the other [32], although further experimentation is needed to verify this observation.

Bibliography

[1] Chen, F. C., Lv, H. Y., Luo, X., Lu, W. J., Pei, Q. L., Lin, G. T., Y. P., Extremely large magnetoresistance in the type-II Weyl semimetal $MoTe_2$. Physical Review B, 94(23), 235154 (2016)

[2] Jiang, J., Liu, Z. K., Sun, Y., Yang, H. F., Rajamathi, C. R., Qi, Y. P. Chen, Y. L., Signature of type-II Weyl semimetal phase in $MoTe_2$. Nature Communications, 8, 13973 (2017)

[3] Sun, Y., Wu, S.-C., Ali, M. N., Felser, C., and Yan, B., Prediction of Weyl semimetal in orthorhombic $MoTe_2$. Physical Review B, 92(16) (2015)

[4] Weng, H., Fang, C., Fang, Z., Bernevig, B. A., and Dai, X., Weyl Semimetal Phase in Noncentrosymmetric Transition-Metal Monophosphides. Physical Review X, 5(1) (2015)

[5] Armitage, N. P., Mele, E. J., and Vishwanath, A., Weyl and Dirac semimetals in three-dimensional solids. Reviews of Modern Physics, 90(1) (2018)

[6] Soluyanov, A. A., Gresch, D., Wang, Z., Wu, Q., Troyer, M., Dai, X., and Bernevig, B. A., Type-II Weyl semimetals. Nature, 527(7579), 495–498 (2015)

[7] Huang, L., McCormick, T. M., Ochi, M., Zhao, Z., Suzuki, M.-T., Arita, R., Kaminski, A. Spectroscopic evidence for a type II Weyl semimetallic state in $MoTe_2$. Nature Materials, 15(11), 1155–1160 (2016)

[8] Yang, J., Colen, J., Liu, J., Nguyen, M. C., Chern, G., and Louca, D., Elastic and electronic tuning of magnetoresistance in $MoTe_2$. Science Advances, 3(12), eaao4949 (2017)

[9] Md Sabbir Akhanda, Sergiy Krylyuk, Diane A. Dickie, Albert V. Davydov, Fei Han, Mingda Li, Mona Zebarjadi, Phase-transition-induced Thermal Hysteresis in Type-II Weyl Semimetals $MoTe_2$ and $Mo_{1-x}W_xTe_2$, Material Physics Today, 29, November 19 (2022)

[10] Kim, H.-J., Kang, S.-H., Hamada, I., and Son, Y.-W., Origins of the structural phase transitions in $MoTe_2$ and WTe_2. Physical Review B, 95(18) (2017)

[11] Schneeloch, J. A., Duan, C., Yang, J., Liu, J., Wang, X., and Louca, D., Emergence of topologically protected states in the $MoTe_2$ Weyl semimetal with layer-stacking order. Physical Review B, 99(16) (2019)

[12] Tao, Y., Schneeloch, J. A., Duan, C., Matsuda, M., Dissanayake, S. E., Aczel, A. A., Louca, D., Appearance of a T_d* phase across the T_d–1T′ phase boundary in the Weyl semimetal $MoTe_2$. Physical Review B, 100(10) (2019)

[13] S. Song, D. H. Keum, S. Cho, D. Perello, Y. Kim, Y. H. Lee, Room temperature semiconductor–metal transition of $MoTe_2$ thin films engineered by strain. Nano Lett. 16, 188–193 (2016)

[14] Tao, Y., An Investigation of the Structural Phase Transitions in a Weyl Semimetal Using Neutron Scattering, Ph.D. thesis, University of Virginia (2022)

[15] Zhu, Z., Lin, X., Liu, J., Fauqué, B., Tao, Q., Yang, C., K., Quantum Oscillations, Thermoelectric Coefficients, and the Fermi Surface of Semimetallic WTe_2. Physical Review Letters, 114(17) (2015)

[16] Yun Wu, Na Hyun Jo, Masayuki Ochi, Lunan Huang, Daixiang Mou, Sergey L. Bud'ko, P. C. Canfield, Nandini Trivedi, Ryotaro Arita, and Adam Kaminski, Temperature-Induced Lifshitz Transition in WTe_2, Phys. Rev. Lett. 115, 166602 (2015)

[17] Yang, J., Colen, J., Liu, J., Nguyen, M. C., Chern, G., and Louca, D., Elastic and electronic tuning of magnetoresistance in $MoTe_2$. Science Advances, 3(12), eaao4949 (2017)

[18] Qi, Y., Naumov, P. G., Ali, M. N., Rajamathi, C. R., Schnelle, W., Barkalov, O., Medvedev, S. A., Superconductivity in Weyl semimetal candidate $MoTe_2$. Nature Communications, 7, 11038 (2016)

[19] Zhu, Z., Lin, X., Liu, J., Fauqué, B., Tao, Q., Yang, C., Behnia, K., Quantum Oscillations, Thermoelectric Coefficients, and the Fermi Surface of Semimetallic WTe_2. Physical Review Letters, 114(17)(2015)

[20] Luo, X., Chen, F. C., Zhang, J. L., Pei, Q. L., Lin, G. T., Lu, W. J., Y. P., T_d-$MoTe_2$: A possible topological superconductor. Applied Physics Letters, 109(10), 102601 (2016)

[21] J. Chadwick, The Neutron and Its Properties, BJR 6, 24 (1933)

[22] B. T. M. Willis and C. J. Carlile, Experimental Neutron Scattering (Oxford University Press, 2017)

[23] Z. Yamani, Z. Tun, and D. H. Ryan, Neutron Scattering Study of the Classical Antiferromagnet MnF_2: A Perfect Hands-on Neutron Scattering Teaching Course Special Issue on Neutron Scattering in Canada., Can. J. Phys. 88, 771 (2010)

[24] G. Shirane, S. M. Shapiro, and J. M. Tranquada, Neutron Scattering with a Triple-Axis Spectrometer: Basic Techniques (Cambridge University Press, 2002)

[25] M. Grimaldo, F. Roosen-Runge, F. Zhang, F. Schreiber, and T. Seydel, Dynamics of Proteins in Solution, Quarterly Reviews of Biophysics 52, e7 (2019)

[26] Stan, C., Beavers, C., Kunz, M., and Tamura, N., X-Ray Diffraction under Extreme Conditions at the Advanced Light Source. Quantum Beam Science, 2(1), 4 (2018)

[27] Dahal, R., Deng, L. Z., Poudel, N., Gooch, M., Wu, Z., Wu, H. C., Chu, C. W., Tunable structural phase transition and superconductivity in the Weyl semimetal $Mo_{1-x}W_xTe_2$. Physical Review B, 101(14) (2020)

[28] Ali, M. N., Xiong, J., Flynn, S., Tao, J., Gibson, Q. D., Schoop, L. M., R. J., Large, non-saturating magnetoresistance in WTe_2. Nature, 514(7521), 205–208 (2014)

[29] Yan, X.-J., Lv, Y.-Y., Li, L., Li, X., Yao, S.-H., Chen, Y.-B., Chen, Y.-F., Investigation on the phase-transition-induced hysteresis in the thermal transport along the c-axis of $MoTe_2$. Npj Quantum Materials, 2(1) (2017)

[30] Abedin, S.; Kurtash, V.; Mathew, S.; Thiele, S.; Jacobs, H.O.; Pezoldt, J., Defects Contributing to Hysteresis in Few-Layer and Thin-Film MoS_2 Memristive Devices. Materials, 17, 1350 (2024)

[31] Heikes, C., Liu, I.-L., Metz, T., Eckberg, C., Neves, P., Wu, Y., Ratcliff, W., Mechanical control of crystal symmetry and superconductivity in Weyl semimetal $MoTe_2$. Physical Review Materials, 2(7) (2018)

[32] Huang, F.-T., Joon Lim, S., Singh, S., Kim, J., Zhang, L., Kim, J.-W.,Cheong, S.-W. (2019). Polar and phase domain walls with conducting interfacial states in a Weyl semimetal MoTe2. Nature Communications, 10(1). doi:10.1038/s41467-019-11949-5